On the Sources of Cold and Dense Plasma in Plasmasphere Drainage Plumes

Naomi Maruyama[1,2], Michael H. Denton[3,4], Yukitoshi Nishimura[5], Michael G. Henderson[6], Philip G. Richards[7], Mariangel Fedrizzi[1,2], Anthea Coster[8], Jacques Middlecof[9,10], Timothy J. Fuller-Rowell[1,2], Mark Govet[10], and Joachim Raeder[11]

[1]Cooperative Institute for Research in Environmental Sciences, University of Colorado, Boulder, CO 80305, USA.

[2]Space Weather Prediction Center, National Oceanic and Atmospheric Administration, Boulder, CO 80305, USA.

[3]Center for Space Plasma Physics, Space Science Institute, Boulder, CO 80301, USA.

[4]New Mexico Consortium, Los Alamos, NM 87544, USA.

[5]Boston University, Boston, MA, USA.

[6]ISR-1, Los Alamos National Laboratory, Los Alamos, NM 87545, USA.

[7]Department of Physics and Astronomy, George Mason University, Fairfax, VA, USA.

[8]Haystack Observatory, MIT, MA, USA

[9]Cooperative Institute for Research in the Atmosphere, Colorado State University, Fort Collins, CO, USA.

[10]Global Systems Division, National Oceanic and Atmospheric Administration, Boulder, CO 80305, USA.

[11]University of New Hampshire, Durham, NH, 03824, USA.

Corresponding author: first Naomi Maruyama (Naomi.Maruyama@noaa.gov)

Key Points:

- Plumes were simultaneously observed in the ionosphere, plasmasphere and near the dayside magnetopause.
- Ionospheric SED plumes were magnetically conjugate features, but their magnitude and structures were not.
- A larger storm does not necessarily have larger plume peak density in the ionosphere and plasmasphere.

Abstract

Previous observations have revealed that the ionospheric Storm Enhanced Density (SED) plumes are colocated with the cold, dense plumes observed at the dayside magnetopause. However, the origin of the cold, dense plume plasma is not well understood with multiple possible sources in the magnetosphere. Improving our understanding of these plasmaspheric plumes is crucial due to their impact on the dayside magnetic reconnection. We report that plumes were simultaneously observed in both the ionosphere and plasmasphere by TEC and geosynchronous spacecraft for the magnetic storms occurred in 2013 and 2015 on Mar 17. Moreover, in 2015, the plume was also observed by THEMIS spacecraft near the dayside magnetopause. Simulations using a physics-based model of the ionosphere and plasmasphere reproduced the observed plume colocation in the ionosphere and plasmasphere for both storms. Our results suggest that plasmaspheric plume was created by the enhanced convection transporting the plasma sunward that was peeled off from the outer plasmasphere, whereas the ionospheric plume plasma came from the density enhancement generated in the dayside subauroral ionosphere. These plumes were observed near the same closed field lines at the peak of the geomagnetic activity because the cold plasma motion in the ionosphere and plasmasphere is connected through the ExB drift motion. Furthermore, our results suggest that weaker storms transport more plasmaspheric materials toward the dayside/duskside magnetopause. However stronger storms may have a larger impact on the dayside reconnection because plasmaspheric plumes tend to be shifted to the noon MLT sector where dayside reconnections more likely to occur.

Plain Language Summary

The plasmasphere is the region of cold, relatively dense ionized gas (mostly protons and helium ions) that resides on the magnetic field lines close to the Earth. It is the upward extension of cold, dense Earth's ionospheric plasma as the ionosphere had filled the persistently "closed" flux tubes of plasmasphere. Enhanced convection plasma flow during solar storms peels the cold, dense plasma away from the outer plasmasphere to form a plume of plasma that moves sunward. Recently, the plasmaspheric cold, dense plasma has been found near where the Earth's magnetic field first contacts the solar wind, however, where the plasma originates from remains unclear. Understanding the plume plasma is very important because they could rearrange the magnetic topology by altering the rate of the magnetic reconnection, which determines how much solar wind energy gets into the Earth's magnetosphere. Here we report that in two solar storms in 2013 and 2015, plumes were observed simultaneously in both ionosphere and plasmasphere. Our study suggests that the observed plumes in the plasmasphere and ionosphere were mainly created by different mechanisms, but were observed near the same magnetic field lines at the peak of the solar storms.

1 Introduction

The plasmasphere is the near-corotating region of cold (~eV), relatively dense (~1000cm^{-3}) ionized gas (mostly protons and helium ions). It is the upward extension of cold, dense ionospheric plasma that exists on the magnetic field lines close to the Earth (within a few Earth radii) (e.g., Carpenter and Park, 1973). During geomagnetically quiet periods, the plasmasphere region expands in size as closed flux tubes slowly fill with cold plasma from the ionosphere.

During more geomagnetically active periods (when IMF B_z turns southward and magnetospheric convection increases), the outer layers of the plasmasphere are stripped away by magnetospheric convection. This enhanced convection leads to a plasmaspheric drainage plume – a spatially constrained region that is cold and dense (>100 cm^{-3}) plasma that is drained from the outer plasmasphere (e.g., Elphic et al., 1996; Borovsky et al., 1998; Thomsen et al., 1998; Borovsky and Denton, 2008). This process is called plasmaspheric erosion (e.g., Chappell et al., 1971; Carpenter et al., 1993; Elphic et al., 1997; Sandel and Denton, 2007). After IMF B_z turns northward and the solar wind driven convection relaxes, plasmaspheric plumes start to corotate with the Earth (e.g., Goldstein, 2006). Plumes are generally very dynamic and their spatial structure and location are highly dependent on the magnitude and time history of the electric fields (e.g., Goldstein et al., 2006; Borovsky and Denton, 2008). These electric fields are generated by the nonlinear interactions between the quiet-time ionospheric wind dynamo process due to solar heating of the dayside Earth's atmosphere, disturbance dynamo due to storm time neutral wind (e.g., Fuller-Rowell et al., 2008), and the sunward convection due to the enhanced solar-wind-magnetosphere interaction (e.g., Maruyama et al., 2011; Ferdousi et al., 2019; Maruyama, 2020).

Su et al. (2001) associated plasmaspheric drainage plumes observed by Los Alamos National Laboratory (LANL) / Magnetospheric Plasma Analyzer (MPA) with polar cap patches in the ionosphere. Patches are regions of enhanced *F*-region plasma density in the form of a series of patches drifting anti-sunward across the polar cap. A continuous stream of such elevated density *F*-region plasma is usually termed the polar tongue of ionization (TOI). The TOI extends out of the elevated dayside midlatitude ionosphere through the cusp and into the polar cap by enhanced convection flows (Sato, 1959; Sato and Rourke, 1964; Knudsen, 1974). The source of the plasma in a TOI can come from an enhancement of ionospheric *F*-region density and total electron content (TEC) at midlatitude in the dusk MLT sector during a positive phase of ionospheric storms, which was originally called "the dusk effect" (Mendillo et al., 1970). The region of the elevated dayside midlatitude ionosphere has also been termed Storm Enhanced Density (SED) (Foster, 1993). Foster et al. (2002) showed that an ionospheric SED plume mapped onto the low-altitude signature of a plasmasphere drainage plume was possibly connected with storm time erosion of the plasmasphere boundary layer (PBL) (Carpenter and Lemaire, 2004) observed by IMAGE/extreme ultraviolet (EUV) imaging. Foster et al (2005) clarified the relationship between SED plume and TOI: the low latitude SED plume forms a source of the polar tongue of ionization (TOI), when entering into the polar cap near noon. Foster et al. (2014) evaluated the plume sunward flux from both VAP in the magnetosphere and DMSP in the ionosphere. The draining plasmaspheric ions and the entering magnetosheath ions were observed on the same flux tube at the dayside reconnecting magnetopause (Su et al., 2000). More recent studies have reported that a SED plume was observed by Global Positioning Satellite (GPS)-TEC observations when a plasmaspheric drainage plume was observed at the dayside magnetopause by THEMIS (Walsh et al., 2013).

Plasmaspheric plumes and ionospheric plumes are often considered to exist on the same field lines. When interpreting individual plume observations, however, it is not currently understood how plasmaspheric and ionospheric plumes are physically connected (e.g., Krall et al., 2018). Where does the plasmaspheric cold, dense plume plasma observed near the dayside magnetopause originate from? Multiple possible sources in the magnetosphere have been suggested (e.g., Fuselier et al, 2017; 2019). From the perspective of magnetosphere-ionosphere-plasmasphere (M-I-P) coupling processes, understanding of plume formation mechanisms is still

121 incomplete. While several other studies reported that plasmaspheric drainage plumes are nearly
122 magnetically conjugate (e.g., Yizengaw et al., 2008), there is uncertainty around why
123 observations often tend to show a considerable degree of hemispheric asymmetry in SED
124 plumes? In particular, the idea of colocating plasmaspheric and ionospheric plumes does not
125 explain the hemispheric asymmetry (winter hemisphere preference) of SED plumes, but would
126 create SED plumes at essentially the same time in the two hemispheres. Furthermore, the electric
127 field is expected to be the same between the two hemispheres on the closed field lines. For
128 example, Foster and Rideout (2007) found that the position of the steep gradient region at the
129 poleward edge of the SED to be closely aligned in the conjugate hemispheres, whereas the
130 enhancement at the base of the plume, which provides a potential plasma source for the erosion
131 events (e.g., Foster et al., 2005), often is significantly non-conjugate.

132 Magnetic reconnection is the primary process through which energy couples between the solar
133 wind and Earth's magnetosphere and ionosphere. It changes the magnetic topology, and converts
134 electromagnetic energy into plasma kinetic and thermal energies. Cold, dense plasmaspheric
135 plumes have already been shown to impact the dayside magnetic reconnection rate near the
136 magnetic reconnection site, both theoretically and observationally (e.g., Borovsky and Denton,
137 2006; Cassak and Shay, 2007; Borovsky et al., 2008; 2013, Cassak and Fuselier, 2016).
138 However, there remains an outstanding question as to under what conditions do plasmaspheric
139 drainage plumes actually participate in the dayside reconnection. This has yet to be answered in
140 any detail.

141 Plumes are known to play three important roles in geospace. First, plume plasma has been
142 observed by spacecraft against the magnetopause (Elphic et al., 1996) and at the dayside
143 reconnection site (Borovsky et al., 1997; Su et al., 2000; Walsh et al., 2013; Fuselier et al.,
144 2016). Understanding of plume formation properties (e.g., timing, location, duration, and size)
145 contributes to the understanding of dayside magnetic reconnection properties (e.g., Borovsky et
146 al., 2008; Walsh et al., 2013; Ouellette et al., 2016). Second, the plasmaspheric plumes are the
147 site of enhanced pitch angle scattering of radiation belt electrons during geomagnetically active
148 times. Thus, understanding the behavior of these plumes is crucial to accurately predict radiation
149 belt behavior. During geomagnetic storms, there is almost certainly some cold, dense plasma on
150 all L shells inside geosynchronous orbit. Hence during storms, plasma waves that favor dense
151 cold plasma can potentially reside at all L shells. These plasma waves may impact the scattering
152 and energization of radiation-belt particles. Finally, the ionospheric electron density structures
153 associated with SED plumes, TOI, polar cap patches have been closely related to plasma
154 irregularities and instabilities and the subsequent radio signal scintillations in the high-latitude
155 ionosphere (e.g., Moen et al., 2013).

156 The primary objective of this study is to understand where the cold and dense plume plasma
157 observed near the dayside magnetopause originates from. What is the formation mechanism that
158 controls the observed apparent connection of plumes between the magnetosphere, plasmasphere,
159 and ionosphere (M-P-I). We report the plumes simultaneously observed by ground-based GPS-
160 TEC (Section 3.1) and Los Alamos (LANL) Magnetospheric Plasma Analyzer (MPA) in
161 geosynchronous orbit (Section 3.2) in both the ionosphere and plasmasphere, for the two storms
162 happened on the same day, 17 March, two years apart, 2013 and 2015, the so called St Patrick's
163 Day storms (Section 2). Furthermore, in 2015, all three THEMIS spacecraft observed the
164 plasmasphere drainage plume plasma being transported to the dayside magnetopause (Section 4.1).

The observed SED plumes were magnetically conjugate in the ionosphere. The numerical simulations using a physics-based model of the ionosphere and plasmasphere, Ionosphere-Plasmasphere-Electrodynamics (IPE) model (Section 3.4), reproduce the observed plumes in both ionosphere and plasmasphere for both storms (Section 4.2). In Section 4.3, dependence of plumes on geomagnetic activity is discussed by comparing the plumes between the two storms. Section 5 includes discussions of the results and their implication in terms of the geospace response to solar wind magnetosphere interactions.

2 Event Description

2.1. Overview of the events

We studied two events covering the period of 17 Mar 2013 and 2015 (KpMax 7^- and KpMax 8^-, respectively), the St. Patrick's Day storms, both of which were associated with Coronal Mass Ejections (CMEs) ejected on 15 March. In 2015, the IMF was strengthened (as well as the subsequent geoeffectiveness) most probably by high speed streams (HSS) from coronal holes compressing the Interplanetary CME (ICME) ahead of the HSS. These events have been extensively analyzed. These storms were chosen since they were relatively strong (SYM-H min ~–130 nT in 2013 and ~223 nT in 2015), and since the SED plume activity was previously documented for 2013 (Foster et al., 2014) and 2015 (Liu et al., 2016). We could thus expect to carry out a useful comparison/contrast since the events occurred on the same day of the year with the same season and with similar solar EUV flux conditions.

2.2. 2013-03-17

Figure 1a shows Interplanetary Magnetic Field (IMF) measured at L1 (~1.42×10^6 km from Earth, time-shifted to the sub-solar magnetopause location) in GSM from the OMNI data set for 17 March 2013. Two forward interplanetary shocks were reported on 15 March at 0442UT and 17 March at 0527 UT (Guerrero et al., 2017). The second IP shock was stronger, driven by an ICME. Subsequently, IMF $\boldsymbol{B_z}$ first fluctuated between south and north, and then turned predominantly southward at ~0550 UT associated with the sudden increase in the solar wind velocity by ~300 km/s (from less than 450 km/s to over 700 km/s caused by the interplanetary shock) and remained mostly southward until ~2120 UT. The IMF turned northward toward the end of the day. SYM-H in Figure 1a shows gradual decrease after the storm commencement at ~0604 UT identified by the sudden positive increase and reached -100 nT at ~1020 UT associated with the strong southward IMF $\boldsymbol{B_z}$. Subsequently the IMF remained nearly constant until ~1900 UT when it dropped again to –132 nT at ~2100 UT, showing the double dip feature during the main phase of this storm. The corresponding increase in the cross polar cap potential (CPCP) in excess of ~200 kV at ~0900 UT is shown in the third panel of Figure 1a. The CPCP values were calculated by using the Weimer convection model (1996). This polar cap potential pattern was used to drive the plasma transport perpendicular to magnetic field lines in IPE. The

CPCP value slowly decreased, followed by the constant value of ~130kV for ~4hours (1500—1930UT) toward the time when the SYM-H reached the minimum value at ~2100UT.

2.3. 2015-03-17

In contrast, for 17 March 2015 as shown in Figure 2a, IMF Bz first turned northward at 0430UT coupled with an observed interplanetary shock at 0400UT. The corresponding solar wind velocity increased by ~100 km/s, followed by the first southward turning at ~0530 UT from ~+20 nT to ~–20 nT and remained mostly southward at ~-20 nT until ~0930UT. The corresponding increase in the CPCP in excess of ~200 kV between ~0600 and 0930 UT. This was followed by a ~3 hour of the northward period, after which the IMF Bz slowly turned southward again at ~1145UT and remained mostly southward at ~–20 nT until the end of the day. SYM-H in panel 2b show a gradual decrease at 0550UT and reaching -80 nT at ~0930 UT at the end of the 1st excursion of the IMF Bz southward. Subsequently SYM-H started decreasing again steadily until ~2245 UT when it dropped to the minimum value of –223 nT. The corresponding CPCP value reached maximum of ~270kV at ~1400UT. The CPCP value remained high (~200kV) until the end of the day. The SYM-H excursion for the 2015 event also indicates double dips during the main phase of this storm which is larger than 2013. The detailed overview description of these events can be found in previous papers (e.g., Raeder et al., 2016; Ferdousi et al., 2019).

3. Data, and Model

3.1. THEMIS:

In situ observations from the Time History of Events and Macroscale Interactions (THEMIS) satellite are used in this study to identify the plumes that are transported toward the dayside magnetopause. Only data for the 2015 event are used because the spacecraft orbit did not detect the plume in the 2013 event. The inner three THEMIS satellites (TH-A, D, and E) successively passed through the dayside magnetosphere approximately along the same orbit between 15 and 21 UT. We use fluxgate magnetometer (FGM) (Auster et al., 2008) magnetic field measurements and onboard plasma moments (MOM) from the Electrostatic Analyzer (ESA) instrument (McFadden et al., 2008) with 3 s cadence. For detecting sunward plasma convection, we use the *Y* component of the electric field (E_y) from the Electric Field Instrument (EFI) (Bonnell et al., 2008), whose noise level is normally small enough (<0.1 mV/m) to detect magnetospheric large-scale electric fields (>1 mV/m). The sunward electric field (E_x) is often affected by artificial offsets and is not suitable for convection studies, but is not critical in this study for detecting sunward convection. The plasmaspheric drainage plume is identified from the electron density derived from the EFI by using the spacecraft potential (Nishimura et al., 2013). Hence, the obtained density is basically a total density from all energies including cold plasma. Our assumption is that during plume observations (density>100cm^{-3}) the cold plasma dominates the density reported by EFI. The usage of the satellites allowed us to distinguish spatial and temporal variations. All satellite data mentioned above are publically available through CDAWeb (cdaweb.sci.gsfc.nasa.gov).

3.2. LANL MPA:

Cold ion density data obtained from the Los Alamos National Laboratory (LANL) Magnetospheric Plasma Analyzer (MPA) were used to identify plasmaspheric drainage plumes. Cold ion density data are obtained by analyzing the measurements from the multi-spacecraft MPA instruments (Bame et al., 1993) in geosynchronous orbits (6.6 R_E) close to the geographic equator. The MPA instruments are spherical sector electrostatic analyzers that measure the three-dimensional velocity space distributions of ions and electrons over the nominal energy per charge range of ~1 eV/q to 40 eV/q. A sequence of two- and three-dimensional ion and electron distributions is measured every 86s. Of the 8 different data products accumulated over this time period, 2 full 3D ion distributions and 1 full 3D electron distribution are acquired. Each of these 3D data products (40 energies × 24 azimuths × 6 polar angles) require a 10.24s time period to assemble. Relative to the start of each 86s cycle, the first 3D ion distribution is measured first, the first 3D electron distribution is measured starting at ~21.5s, and the second 3D ion distribution is measured starting at ~53.25s. Further details on the instrument are provided by Bame et al. (1993), McComas et al. (1993), and Thomsen et al. (1999). In contrast to most other platforms, the geosynchronous spacecraft charge negatively with respect to the ambient plasma enabling efficient analysis of the cool-ion populations of the magnetosphere. A detailed analysis of this negative spacecraft charging is found in Borovsky et al. (1998) and Thomsen et al. (1999). In this study, moments of the distributions of plasmaspheric ions are used, specifically the number density and flow velocity. MPA instruments do not measure the ionic composition of the plasmasphere, which is known to vary with $F_{10.7}$ and with the solar cycle (Brace et al., 1968; Newberry et al., 1989; Craven et al., 1997). However, under certain circumstances, the ion composition can be inferred from MPA and such analysis confirms the variations with F10.7 and solar cycle (Denton et al., 2005). Furthermore, the MPA instruments do not measure the charge state of the ions, either. Moments of the measured distributions are produced by assuming all ions collected are protons (Thomsen et al., 1999). Borovsky and Denton (2008) estimated that the actual plasma number density would be 1.21 times the value produced by MPA if the ionic composition of the plasmasphere were 70% H^+, 20% He^+, and 10% O^+ (e.g., Figure 4.8 of Lemaire and Gringauz, 1998). Furthermore, the actual flow velocities would be 0.825 times the MPA-produced flow velocities for the same ionic composition. Borovsky and Denton (2008) also revealed a systematic picture of the gross behavior of the plasmasphere and the drainage plumes as a function of geomagnetic activity that largely agrees with the models and previous simulation results (e.g., Lambour et al., 1997; Weiss et al., 1997; Liemohn et al., 2006; Jordanova, 2006), by analyzing the decades of observations of the cold plasma by MPA.

3.3. GPS-TEC:

GPS TEC data are used to detect ionospheric SED plumes and TOIs in 2D TEC maps in this study, and to add context to the sparse in-situ measurements in the magnetosphere. Two dimensional maps of TEC are commonly used to depict the highly variable nature of the F-region ionosphere, including SED plumes, TOI, and patches (e.g., Thomas et al., 2013). Researchers at MIT Haystack Observatory generate maps of vertically integrated TEC from a global network of GPS receivers and offer their data product to the larger scientific community via the Madrigal database. The GNSS processing algorithms used at Haystack were originally developed by (Rideout and Coster, 2006). Recently, new TEC processing algorithms have been implemented for better bias estimation and inclusion of GLONASS data (Vierinen et al., 2015). The TEC measurements of the ionosphere describe the total number of electrons contained in a

cylinder of cross-sectional area $1m^2$ that extends vertically above a given point on the Earth and extends all the way through the ionosphere. One TEC unit (TECU) is given as 1×10^{16} electrons/m^2; typical peak dayside values can range from less than 10 TECU on a quiet day to the hundreds of TECU observed during strong geomagnetic storm activity. Measurements are binned into 1deg × 1deg cells at 5 min resolution. SED plumes observed in GPS-TEC data were identified as channels of enhanced TEC distinctly larger than the surrounding area, extending poleward by >~5 deg out of dayside solar EUV ionized plasma at midlatitudes. When receivers cover the dayside mid- to high-latitude ionosphere (typically 8–24 UT in the Northern Hemisphere), TOIs are the extension of those extending toward the magnetic pole region. The time integration of the TEC data was made for 15 min in order to increase spatial coverage of one image: this is reasonable to study SED plumes since they typically last longer than ~30 min.

3.4 The Ionosphere Plasmasphere Electrodynamics (IPE) Model

3.4.1. Overview

A physics-based model of the ionosphere and plasmasphere, The Ionosphere Plasmasphere Electrodynamics (IPE) model (Maruyama et al., 2016; Sun et al., 2015; Obana et al., 2019), is used to understand the underlying processes that physically connect the observed plumes between the ionosphere and plasmasphere. The IPE model is a time-dependent, global, three-dimensional fluid model of the ionosphere and plasmasphere. It provides time-dependent, global, three-dimensional plasma densities for nine ion species, thermal electron and ion temperatures, and both parallel and perpendicular velocities of the ionosphere and plasmasphere. A unique feature of the IPE model is global implementation of a more accurate representation of the Earth's magnetic field in conjunction with the well-tested Field Line Interhemispheric Plasma (FLIP) model (e.g., Richards et al., 2010) for the parallel plasma transport along field lines. The realistic representation of the Earth's magnetic field combined with the self-consistent photoelectron calculation (described in a later section) enables more accurate studies of the longitudinal and UT dependencies and hemispheric asymmetry that are crucial for this study. The interhemispheric field lines in IPE have three-dimensional, global coverage from the magnetic equator to the pole, which allows for the global seamless plasma transport perpendicular to magnetic field lines.

3.4.2. Apex Coordinates within magnetic flux tubes

In the original FLIP model, the Earth's magnetic field has been assumed to be a tilted dipole approximation. In reality, however, the low-latitude geomagnetic field departs from the dipole equator by more than 10 degrees over the Atlantic Ocean and Africa. Furthermore, the ionospheric electric field calculation depends on the strength of the magnetic field, since the wind-driven currents depend on the field line integration of the ionospheric conductivity and neutral wind. IPE uses the Apex coordinates (Richmond, 1995) based on the International Geomagnetic Reference Field (IGRF)-10 (Maus et al., 2005). We have implemented the Apex coordinates into a flux tube-type ionosphere plasmasphere model, FLIP. When implementing the Apex coordinates, we included the new and modified definition of the orthogonal curvilinear coordinate system (p, q, ϕ) (Kendall, 1962) which has been used for the dipole magnetic field approximation (Bailey and Balan, 1996; Huba, 2000).

$$p_D = \frac{\mathrm{r}}{r_e \sin^2\theta} \quad (1)$$

$$q_D = \frac{r_e^2 \cos^2\theta}{r^2}, \quad (2)$$

where r_e is the Earth radius, and r is the distance from the center of the Earth. Note that ϕ is the same longitudinal coordinate as in the original spherical polar coordinates.

$$\boldsymbol{\eta_D = \frac{1\left(1+3\cos^2\theta\right)^{1/2}}{r_e}\left(\frac{r_e}{r}\right)^3} \quad \textbf{(3)}$$

$$\boldsymbol{\frac{\partial}{\partial s_D} = \eta_D \frac{\partial}{\partial q_D}}, \quad \textbf{(4)}$$

where S_D is the arc length along a field line. In the IPE, the Apex coordinates, (p_A, q_A, ϕ) becomes as follows:

$$p_A = \frac{1}{\cos^2\lambda_m} \quad (5)$$

$$q_A = -\frac{V_0}{V_p}, \quad (6)$$

where λ_m is the definition of the magnetic latitude in the Apex coordinates as defined in equation (3.3) in Richmond (1995), V_0 is the magnetic potential at each grid point, V_P is a constant parameter, approximately the magnetic potential value at the south pole at the reference altitude, that is 90 km in the case of IPE model.

$$\eta_A = -\frac{B_0}{V_p}. \quad (7)$$

In the dipole coordinate system, the value q=0 defines the magnetic equator with negative values of q in the Southern hemisphere and positive values in the northern hemisphere, whereas in the new Apex coordinates, the value of q does not necessarily equal to zero. The plasma transport in the new Apex coordinates follows along the new q values both in parallel and perpendicular directions. The following section explains the plasma transport in this new Apex coordinates, (p_A, q_A, ϕ) coordinates in the flux tube type grid in IPE.

3.4.3. Parallel Plasma Transport: FLIP

3.4.3.1. FLIP Basic Equations

The plasma transport of IPE parallel to magnetic field lines is based on the well-tested, one-dimensional flux-tube based model, Field Line Interhemispheric Plasma (FLIP) model (Richards et al., 2010). It has evolved continuously over more than 30 years as a tool specifically designed to improve our understanding of the physics and chemistry of the ionosphere and plasmasphere. It solves for equations of continuity and momentum for the two major species (O^+, H^+) and the two minor species (He^+, and N^+), energy equations for electrons and ions along entire magnetic flux tubes from 90 km in the northern hemisphere through the plasmasphere to 90 km in the southern hemisphere (Young et al., 1980a,b; Torr et al., 1990). The same solver is used all the way from the equator to the pole with no boundary conditions inside the solver in a global static grid. The solution procedure allows complete flexibility in setting up the field line grid spacing.

3.4.3.2. Photoelectron Flux Calculation

FLIP accounts for heating of the topside ionosphere by photoelectrons that travel significant distances away from where they are generated encompassing the entire field line on the same spatial grid as the ion continuity and momentum equations (Torr et al.,1990). It solves for the photoelectron transport equations using the two-stream approach, based on the method of Nagy and Banks (1970), including thermal electron heating due to photoelectrons, secondary ion production and conjugate effects. Trapping of photoelectrons can be included by specifying trapping fractions that determine the amount reflected from a nominal height of 1000 km (Richards and Torr, 1990). However, in this study, no pitch angle trapping effect was included. In IPE, the equations are solved in the Apex coordinates, including a more realistic magnetic field, which, if in sunlight, allows photoelectron heating from the opposite hemisphere in a more realistic manner, enabling us to evaluate universal time and longitudinal dependences more accurately.

3.4.4. Perpendicular Transport

Instead of directly solving the equations, the perpendicular transport of the plasma is determined from the conservation laws for mass and magnetic flux caused by moving the plasma across the magnetic field by **E×B** drift. In order to include the motion of plasma perpendicular to the geomagnetic field, the globally distributed interhemispheric flux tubes in the model have to move under the influence of electric fields driven by the plasma **E×B** drift. A global static grid (i.e., plasma moves across the fixed flux tube grid) with a semi-Lagrangian scheme (Fuller-Rowell et al., 1987) is implemented, as used in the Coupled Thermosphere Ionosphere Model (CTIM) (Fuller-Rowell et al., 1996) and Coupled Thermosphere Ionosphere Plasmasphere electrodynamics (CTIPe) model (Millward et al., 2001), since the Lagrangian scheme would have required an enormous amount of effort to keep track of trajectories of all the moving flux tubes, in particular, when applied to geomagnetically active conditions with enhanced electric fields. Furthermore, the semi-Lagrangian scheme has an advantage of allowing for larger time steps (e.g., ~15 min for geomagnetically quiet periods) than the Eulerian-based advection schemes, with no loss of accuracy (Staniforth and Cote, 1991).

The horizontal grid (magnetic longitude, latitude) is used to estimate the departure point at the previous time step, $t = t$ - delta t. An imaginary flux tube at the departure point at the previous time step is created and the state variables at each grid point of the imaginary flux tube is interpolated using the information on the neighboring flux tubes. The state variables on the imaginary flux tube are used to solve the equations for the current time step, $t = t$. The description of the conservation laws for mass, energy and magnetic flux caused by the moving the plasma across the magnetic field is based on Richards (1979).

Implementation of a global static grid allows for a global seamless transport that uses the same parallel transport solver (FLIP) all the way from the equator to the pole. The perpendicular transport is updated every 10 sec in this study (which depends on magnitudes of plasma flow), while the parallel transport (the calling frequency of the FLIP module) is every 60 sec.

3.4.5. Solar EUV

Photoionization rates and photoelectron fluxes are calculated by using the combination of the solar EUV irradiance model for aeronomic calculations EUVAC (Richards et al., 1994) and HEUVAC (Richards et al., 2006). HEUVAC is a high-resolution version of EUVAC, including

the irradiances below 50Å that are important for photoelectron production. Photoionization and photoelectrons are treated separately because photoelectron calculations need higher resolution. The fluxes in the two models are the same down to 50 Å. Solar EUV irradiance measurements from the SNOE and TIMED satellites support the basic HEUVAC irradiances (Richards et al., 2006). In both models, the irradiance in each wavelength bin is driven by functions based on the average of the daily observed $F_{10.7}$ and its 81-day running mean.

3.4.6. Thermosphere Models

The thermospheric temperatures and number densities are obtained from the Naval Research Laboratory (NRL) Mass Spectrometer, Incoherent Scatter Radar Extended (NRLMSISE-00) model (Picone et al., 2002). The winds are from the Horizontal Wind Model (HWM93) (Hedin et al., 1996), although the model now has an option to self-consistently couple to the Whole Atmosphere Model (e.g., Akmaev et al., 2008; Fuller-Rowell et al., 2008). The NRLMSISE-00 and HWM93 are driven by the daily observed $F_{10.7}$, its 81-day running mean. The NRLMSISE-00 model also uses the 3-hour AP. The O^+-O collision frequency is important for the calculation of the wind effects. A correction factor (1.0~1.7) to the value based on the theoretical calculation (Banks, 1966) was introduced by Burnside et al. (1987) to reconcile optical and radar wind measurements. This study uses a correction factor of 1.0.

3.4.7. Electric Field Models

The storm time response of the plasmaspheric electron density is realized by the time-dependent, high-latitude drivers of the cross polar cap potential drop (Weimer, 1996). In this study, the global coverage of the electric fields is provided by including the mid- and low-latitude empirical model of Scherliess and Fejer (1999) in order to focus on plasma dynamics in the ionosphere and plasmasphere during magnetically active conditions. The IPE model now has an option to self-consistently calculate the mid- and low-latitude electric potential based on the global ionospheric electrodynamic solver (Richmond and Maute, 2014). The electrodynamic module in IPE solves for the electric current continuity equations described in Richmond (1995). Field-line integrated conductivity and conductivity weighted neutral wind are calculated within the IP module (i.e., equation 5.13–5.20 in Richmond, 1995). The calculated electric fields also are fed back to the plasma transport within the IP module. Note that the field-aligned currents from magnetosphere has not yet been included.

In order to apply the model to the highly dynamical magnetospheric convection, Weimer model is driven by the 1 min solar wind parameters, the corresponding global perpendicular **E×B** transport is updated every 10 sec, while the parallel transport (the calling frequency of FLIP) is every 60 sec.

3.4.8. Auroral Precipitation

Energetic particle precipitation is another physical process that is critical in studying the storm time response of the ionosphere and is considered to have a potential influence on SED plumes and TOI features. Altitude profiles of the auroral particle ionization rate are evaluated based on the statistical maps of auroral electron energy influx and characteristic energy that have been developed by measurements from the TIROS-NOAA polar orbiting satellites (Fuller-Rowell et al., 1987; Evans et al., 1987). The maps are ordered by the hemispheric power index estimated

from the TIROS-NOAA (or DMSP) satellites and specify the two auroral parameters, as functions of magnetic latitude and magnetic local time. Each characteristic energy defines a mean shape of a particle energy spectrum between 300 eV and 100 keV, as illustrated in Figure 1 of Fuller-Rowell and Evans (1987). There are a total of 21 different spectra, one for each characteristic energy. The spectral shape in this part of the auroral spectrum does not necessarily have to assume a Maxwellian distribution, since the instrument observed at multiple energies to enable the energy spectrum to be defined.

An altitude profile of the ionization rate for a given auroral energy influx and characteristic energy deposited into a given neutral atmosphere is calculated assuming an isotropic pitch angle distribution (Rees, 1963; Jones, 1974). In contrast, the effect of the 0–300 eV part of the auroral spectrum is included in the ionization rates by assuming a Maxwellian spectrum in that part of the spectrum with the same mean energy since the energy range is not measured by the TIROS-NOAA instruments.

The total ionization rate at a given altitude is partitioned into the three major species O, O_2, and N_2 based on their mixing ratios. Subsequent partitioning into different ionization ion states is determined by folding the spectra with the actual partial cross sections. Fixed branching ratios based on Richards and Torr (1990) are used in order to minimize computationally expensive full calculations. The list of branching ratios used in the model is as follows: N_2^+ (Doering and Goembel, 1991) (higher levels of N_2^+ are for states that dissociate); N^+ (Richards and Torr, 1985); O^+ from O_2 dissociation (Rapp and Englander-Golden, 1965). Cross sections for the higher energy states of O^+ have not been included yet, even though they are most important for charge exchange with N_2, which converts a large fraction to N_2^+. Note that the fractions may vary with characteristic energy.
The maps of energy flux and characteristic energy are updated every minute by using the solar wind parameter variations, as shown in Figure 1, in order to apply the model to the dynamically varying magnetospheric forcing during the storms.

3.4.9. Model Capabilities

The IPE model has been applied to the investigation of the ionospheric response to terrestrial weather events, such as the sudden stratospheric warmings (SSWs) (Millholland et al., 2013). Furthermore, IPE reproduces the climatological behavior of global TEC, in particular, including the Southern Hemisphere Midlatitude Summer Nighttime Anomaly (MSNA)/Weddell Sea anomaly (WSA) and its apparent eastward motion (Sun et al., 2015). The global ionospheric *F*-region electron density shows remarkable agreement with COSMIC observations with the correlation coefficient of 0.84 (Maruyama et al., 2016). The study suggests the cause of the three-peak structure in the global ionospheric *F*-region electron density. Furthermore, IPE was used to explain the observed severe depletion in the plasmasphere during an intense storm in September 2017 (Obana et al., 2019). Very recently, IPE has been self-consistently coupled to the Whole Atmosphere Model (WAM) (Akmaev and Juang, 2008; Akmaev et al., 2008; Fuller-Rowell et al., 2008) to investigate the connection between terrestrial and space weather. The model coupling has been achieved by using the three-dimensional regridding interfaces of the Earth System Modeling Framework (ESMF) and the NOAA Environmental Modeling System (NEMS) coupling infrastructure (earthsystemcog.org/projects/ufs-coupling) (Theurich et al., 2016). The coupled WAM-IPE model has been delivered to NOAA Space Weather Prediction

Center (SWPC) and has been running 24/7 on the National Weather Service (NWS) operational supercomputers in a test operation mode since October 2017 (Maruyama et al., 2017).

3.4.10. Model Input Parameters

The daily $F_{10.7}$ values were obtained from the National Geophysical Data Center (NGDC) for March 2013, and 2015 to be used in the IPE simulations in this study. Planetary geomagnetic activity index, Ap that is needed to drive MSIS and HWM was set to constant 4. The solar wind parameters that are needed to drive Weimer was obtained from OMNI as shown in Figure 1.

4 Results

4.1. Cold, Dense Plumes at the dayside magnetopause Observed by THEMIS

Figure 2a shows the orbital segment of the THEMIS spacecraft during the interval from 1800 UT to 2000 UT on 17 Mar 2015 in the X-Y plane (left) and X-Z plane (right). During our analysis period, the orbits of the nearly equatorial THEMIS spacecraft enable magnetopause observations over a large range of local time and radial distances. THEMIS had an apogee in the dayside and a perigee in the night side, and flew from the magnetosphere to the magnetosheath toward the dayside magnetopause in the outbound passes of its orbit. Figure 3a–c demonstrates that all three inner THEMIS spacecraft (ThA, ThD, and ThE) detected a long-lasting plume in the dayside magnetosphere and at the magnetopause crossing. Boundary crossings are identified through changes in the ion/electron energy spectra and magnetic field vector (e.g., Walsh et al., 2013). For example, in the ThE observation, inside the magnetosphere the background (plasmatrough) density would have been ~10 cm^{-3} without the plume, while inside the plume the density was elevated more than an order of magnitude greater at ~400 cm^{-3}. Such densities are comparable with LANL/MPA observations at GEO where plume densities are observed > 300 cm^{-3}. As seen near the middle of the plot in the post-noon sector (~12.5 MLT) as the satellites moved outward from 4 to 8 R_E near the magnetospheric equatorial plane (as seen in Figure 3a) at 15:30–21:00UT on 17 Mar 2015. The actual plume might have lasted longer. This cannot be confirmed with the observations as the satellites moved away. The magnetosheath density is less than an order of magnitude at ~30 cm^{-3} as compared to the magnetosphere density with the plume. The hybrid Alfvèn speed (vA) as defined by Cassak and Shay (2007) (which takes into account the asymmetric densities and magnetic field strengths on each side of the magnetopause boundary) is 380 km/s (the density is 50 cm^{-3} inside the magnetopause and 10 cm^{-3} outside the magnetopause) that is close to the measured reconnection flow of 300km/s, while it would have been 860 km/s if no plume existed (density is 10 cm^{-3} inside the magnetopause). These values are within a reasonable range as compared to the evaluation in Walsh et al. (2013) that reported 179 km/s for the plume event, and 393 km/s for the non-plume event. The presence of a plume lowers the Alfvèn speed significantly and also, potentially the dimensionless reconnection rate.
The plume is transported toward the dayside magnetopause (shown by the solid vertical lines) by the dawn-to-dusk electric field (~3mV/m) that corresponds to the sunward flow of ~30 km/s. The plume density appeared to be increased at the higher L value of the peak of the ring current enhancement (ion energy of ~10 keV near L=~5). The plasmaspheric plume also appears to have existed only at L>~5.3 in the THEMIS observation as the spacecraft moved from the prenoon MLT sector (Figure 3a). In the following section, we show that the plume observed in the ionosphere extends continuously from the dusk-to-noon MLT sector.

536
537 **4.2. SED Plume in the Ionosphere**
538 **4.2.1 GPS-TEC observations**
539 SED plumes in the ionosphere were simultaneously identified in the GPS-TEC observation at the
540 magnetic foot point of the THEMIS observations on 17 Mar 2015. The ground-based observations
541 allow us to monitor the large-scale morphology and plays an important role in adding the context
542 to the sparse, in-situ observations in the magnetosphere. Figure 4a–c, illustrates the SED plumes
543 observed by GPS-TEC in the Northern Hemisphere for the St. Patrick's Day storm at 1900UT in
544 2013(a) and at 1930UT in 2015(c). The different times were selected to show the peak time of the
545 plume evolution for each event. The plumes in GPS-TEC were identified as channels of TEC
546 enhanced from surrounding longitudes, extending poleward out of dayside solar EUV ionized
547 plasma at midlatitudes. Note that in 2015, THEMIS 3 footprints A/D/E all surround the SED plume
548 in the observed GPS-TEC.
549 The trough (shown by dark blue) was deeper in 2015 than in 2013. The SED plume extended into
550 the cusp, and over the magnetic pole to form TOI more prominently in 2013 than in 2015 even
551 though the storm in 2015 could be considered to be a more intense storm, in terms of the magnitude
552 of the maximum CPCP. We will discuss the possible cause of the difference between the two
553 storms in Section 5.
554 Comparison between Figure 4a and b illustrates the hemispheric difference observed in GPS-TEC
555 for the St. Patrick's Day storm in 2013. While the TEC enhancements in the SED plume were
556 conjugate features. However, the magnitude and structure of the density enhancement appeared
557 non-conjugate between different hemispheres. We will discuss the hemispheric asymmetry of SED
558 plumes in further detail in Section 5.2.
559
560 **4.2.2 IPE simulations**
561 Figure 5 shows the SED plumes in the Northern Hemisphere obtained by the IPE model
562 simulations for the St. Patrick's Day storms in 2013(a) and 2015(c) at the same time as Figure 4
563 GPS-TEC for the purpose of comparison. The movies of the temporal variations of the two
564 dimensional TEC maps obtained from the IPE model simulations are included as Supplement A.
565 IPE is able to reproduce SED plumes for the St. Patrick's Day storms in both 2013 and 2015. SED
566 plumes in TEC were identified as channels of TEC enhanced from the surrounding longitudes with
567 the decreased density associated with the trough. The expanded convection transports plasma from
568 the dayside sub-auroral latitude to the cusp, and into the polar cap. The plasma density near the
569 base of the SED plumes at the sub-auroral latitude rapidly increases as the geomagnetic activity
570 increases starting at ~0600UT for 2013 and ~0600UT for 2015. The prompt penetration electric
571 field caused by equatorward expansion of convection creates vertical drift (e.g., Maruyama et al.,
572 2005; Maruyama et al., 2007), because of the tilted magnetic field at midlatitude. In the presence
573 of sunlight, small vertical drifts result in a significant decrease in the chemical losses and dramatic
574 increases in TEC (Heelis et al., 2009). The empirical potential pattern derived from the Weimer
575 model that is used in the IPE simulations implicitly includes the equatorward expansion of the
576 convection electric field. In contrast to the observations, the model density enhancement at the
577 sub-auroral latitude is not connected to mid- and low-latitude TEC because the equatorward
578 boundary of the Weimer model is located at 45° magnetic latitude at which the boundary condition
579 of the electric potential is set to zero.

Furthermore, IPE reproduces the difference of SED plumes between 2013 and 2015: SED plume density is smaller in 2015 even though the intensity of the storm is larger in 2015. Furthermore, the IPE model simulations shown in Figure 5a–b successfully capture the hemispheric difference qualitatively even without taking into the hemispheric asymmetry of the magnetospheric forcing (electric potential and auroral precipitation) between the two hemispheres. In the IPE model, only the potential in the Northern Hemisphere was used to describe the plasma transport in the direction perpendicular to the magnetic field in the both hemispheres. This gives an interesting insight, which seems to indicate that the main cause of the hemispheric asymmetry of the TEC maps can be attributed to the background neutral parameters and solar EUV production. Mapping of the TEC maps from geographic to geomagnetic coordinates might also play a role in distorting the structure of the density enhancement.

4.3. Plasmaspheric Drainage Plumes

4.3.1. LANL MPA observations

One might wonder about the connection between the plumes at the dayside magnetopause (THEMIS) and in the ionospheric *F* region (GPS-TEC). Indeed, the plasmaspheric drainage plumes were also observed at geosynchronous when the plumes were observed by both THEMIS spacecraft and GPS-TEC.

Figure 6 shows the cold ion density (a,c) and speed (b,d) observed by MPA instruments onboard the seven spacecraft at geosynchronous orbit (L=6.6) as functions of MLT and Day of Year (DOY) starting from 11 Mar for the same two storms (2013-03-17 and 2015-03-17). The density suddenly dropped at ~1200UT on 17 Mar in both the 2013 and 2015 events, which indicates plasmaspheric erosion. At the same time, the cold ion speed increased around the noon MLT sector, as convection becomes stronger as the storms progress. The cold ion velocity vector plot in Figure 7 shows sunward flow of ~25 km/s, which is comparable to the THEMIS dawn-to-dusk electric field of ~3 mV/m shown in Figure 2. Furthermore, the plume-like features (as indicated by the enhanced density) are observed around the noon MLT sector for both storms. These observations indicate that the plume is being transported to the dayside magnetopause by the sunward flow.

Note that here the observed MPA density (<~100 cm^{-3}) is in general underestimated as compared to that of THEMIS (~400 cm^{-3} in plumes) since the MPA moment calculation assumes all the ions are protons, while there could be a significant contribution from higher mass-density ions.

4.3.2. IPE model simulations of the Plasmaspheric Drainage Plumes

The IPE model was used to simulate the response of the plasmasphere to the two St Patrick's Day storms. The IPE model simulations in Figure 8 capture the sudden decrease of the cold ion density (the color change from green to blue) at ~1300UT of 17 Mar in both 2013 (Figure 8a) and 2015 (Figure 8b), at the same time as the observed plasmaspheric erosion. The plume type features near noon MLT sector is also reproduced by IPE. As shown in Figure 9, the equatorial electron density at the magnetospheric equatorial plane exhibits the plume type features near the noon MLT, at the same time as the SED plumes in TEC in Figures 4 and 5. The plume type structures near noon MLT in Figures 6, 7, 8, and 9 indicate that the plasmaspheric drainage plumes convect toward the dayside magnetopause due to the enhanced sunward convection, also evident in the data shown in Figure 7. The Supporting Information 2 shows a movie of the simulated 24-hr variation of plasmaspheric electron density for 17 March 2013 and 2015. The plasmasphere is originally full and saturated. The plasmasphere gets eroded as the storm

626 convection increases. Azimuthal flow transports plasma from the nightside toward noon and
627 radial flow transports plasma sunward resulting in plasmaspheric drainage plumes convecting
628 toward the dayside magnetopause. The plasmaspheric erosion and drainage plume are more
629 distinct in 2015 because of the stronger convection indicated by the electric potential (the white
630 line contours).
631 Comparison of the plasmaspheric drainage plumes between 2013(a) and 2015(b) in Figure 8
632 shows that the peak plume density is higher in 2013 (KpMax=7^-) than that of 2015 (KpMax=8^-),
633 which is consistent with the SED plume density in TEC, as shown in Figures 4 and 5.
634 Furthermore, the plasmaspheric drainage plume locations shift toward local noon for the stronger
635 storm. In the IPE simulation results in Figure 8, the plasmaspheric drainage plume also shifts
636 closer to noon in 2015 (Figure 8b), while in 2013 (Figure 8a), the plume shifts toward dusk.

637 **5. Discussions and Conclusions**

638 In order to address the main science question, "where does cold and dense plume plasma
639 observed near the dayside magnetopause originate from?," we studied the two St. Patrick's Day
640 storms, 17 Mar in 2013 and 2015, by combining the multiple observations and physics-based
641 model simulations. Our findings are as follows: (a) plumes in the ionosphere, plasmasphere, and
642 dayside magnetopause are connected for the two storm cases; (b) ionospheric SED plumes
643 appeared magnetically conjugate for the 2013 event; (c) the peak density of the plasmaspheric
644 drainage plume is smaller for the 2015 stronger storm. The plume location is shifted more toward
645 noon MLT for the stronger storm.
646
647 **5.1. What Process Determines the Plume Colocation?**
648 The plumes were observed both in the magnetosphere and ionosphere (here referred to as
649 colocation). In addition, the physics-based model, IPE, also reproduced the colocation feature.
650 Our results are thus consistent with the previous findings that ionospheric SED plumes can be
651 related to those of the plasmasphere (e.g., Foster et al., 2002, 2014; Yizengaw et al., 2008).
652 However, from the perspective of the magnetosphere-ionosphere-plasmasphere (M-I-P) coupling
653 processes, understanding of plume formation mechanisms is still incomplete. Whether plumes
654 are always connected between the ionosphere and plasmasphere remains an open question. For
655 example, Borovsky et al. (2014) reported long-lived plasmaspheric drainage plumes observed by
656 the LANL MPA instruments for as long as 11 days during high-speed-stream-driven storms. It
657 has yet to be clarified whether or not plasma plumes of the ionosphere and plasmasphere are
658 physically connected during this entire period. While ionospheric density anomalies associated
659 with SED and TOI have been observed during CIR-driven storms (e.g., Pokhotelov et al., 2009),
660 the typical duration of ionospheric SED plume observations is several hours (Shunrong Zhang,
661 private communication).
662 Mechanisms suggested in previous studies to explain ionospheric SED plumes includes: (i1)
663 large upward flows combining both **E×B** convection and antiparallel flows (Zou et al., 2013);
664 (i2) horizontal advection due to fast flows, such as those associated with SAPS flow (Foster et
665 al., 1993; 2007; Liu et al., 2016b); (i3) energetic particle precipitation (Yuan et al., 2011); (i4)
666 enhanced thermospheric wind in the topside ionosphere (Zou et al., 2013; Sojka et al., 2012); and
667 (i5) downward ion flux within plumes, possibly caused by altered plasma pressure distribution
668 due to ambipolar diffusion and a wind effect along field lines (Zou et al., 2014).
669 In contrast, the formation mechanisms suggested to explain plasmaspheric drainage plumes are
670 very different from ionospheric SED plumes. Borovsky et al. (2014) provided comprehensive

discussions of: (p1) cold plasma stripped off (or drained) by enhanced convection from plasmaspheric plasma from lower L shells being transported to the dayside to form a narrow channel of dense plasma; (p2) diffusion from the inner magnetosphere due to ULF fluctuating electric fields; (p3) substorm disruptions of the plasmapause (e.g., Henderson et al., 2018); (p4) interchange-type instabilities; (p5) velocity shear driven instabilities; and (6) ionospheric super outflow from inside plumes (Krall et al., 2018). Exactly what physical process controls the plume formation and colocation and their difference between the ionosphere and plasmasphere is still to be determined.

Since our model simulations agree with the observations of GPS-TEC and MPA at least in a qualitative manner, we could attempt to exclude some of the above hypotheses from the essential processes required to form the plumes in the ionosphere and plasmasphere observed on 17 March 2013 and 2015. (i3--4) are not the essential processes as they are not included in the IPE model simulations. Similarly, (p2), (p3), and (p5) are not essential in reproducing the plasmaspheric plumes observed by MPA. However, it is expected that including these processes (precipitation and storm time neutral wind) in the simulations could improve the agreement with the observations. Furthermore, plasmaspheric processes (p2, p3, p5) may play an important role in explaining the observed considerable variability and lumpiness reported in the statistical nature of the observed plumes (Borovsky and Denton, 2008).

5.2. What Process Determines the Hemispheric Asymmetry of Ionosphere SED Plumes?

Plasmaspheric drainage plumes and ionospheric SED plumes are often considered to exist on the same field lines because cold plasma transport in both the ionosphere and plasmasphere is controlled by the same **E×B** drift. Several studies have reported that plasmaspheric drainage plumes are nearly magnetically conjugate (e.g., Yizengaw et al., 2008). However, it is not clear why observations often tend to show a considerable degree of hemispheric asymmetry in ionospheric SED plumes? In particular, the idea of colocating plasmaspheric and ionospheric SED plumes does not explain the hemispheric asymmetry (winter hemisphere preference) of TOIs and patches (e.g., Coley and Heelis, 1998), but would create SED plumes essentially simultaneously in the two hemispheres. The understanding of whether or not ionospheric SED plumes always have magnetically conjugate features remains an open question.

The comparison of the ionospheric SED plumes between the two hemispheres in Figures 4 and 5 demonstrates that, while the TEC enhancements associated with SED plumes are conjugate features, the magnitude and structure of the density enhancement do not appear to be conjugate between different hemispheres. The IPE simulation also reproduces the conjugate features as demonstrated in Figures 5. For example, the SED plume density maximum is located inside the polar cap in the Northern Hemisphere whereas the plume density maximum in the Southern Hemisphere is near the base of the SED plume. Interestingly, our simulation result suggests that using the IGRF magnetic field in the IPE model alone is sufficient to reproduce the observed asymmetry of the ionospheric SED plumes in a qualitative manner. Our result is qualitatively consistent with previous studies as well (e.g., Foster and Rideout, 2007; Heelis et al., 2009). For example, Foster and Rideout (2007) showed that the position of the steep gradient region at the poleward edge of the SED was closely aligned in the conjugate hemispheres, whereas the enhancement at the base of the SED plumes, which provides a plasma source for the erosion events (e.g., Foster et al., 2005), often was significantly non-conjugate. The amount of TEC at the base of the plume is greatest in the American sector, indicating additional plasma sources

resulting from repeatable physical processes in this region, which has been called the "Florida effect" (e.g., Coster et al., 2007). The most effective universal times for TEC enhancement is expected to occur in the Northern Hemisphere near 1900 UT and in the Southern Hemisphere near 0700 UT because the density enhancement is expected to be largest when the longitude region incorporating the magnetic pole is tilted toward the dayside (Heelis et al., 2009; Coster et al., 2016). The supplemental information to this paper includes movies of the IPE simulations support the maximum enhancement in the American longitude sector in the Northern Hemisphere for the two storms. The ionospheric SED plume was observed at ~1900 UT in the Southern Hemisphere, as demonstrated in Figure 4b, even though TEC measurements in the Southern Hemisphere were limited and even though it was outside of the optimum universal time for the Southern Hemisphere. Exactly what causes the hemispheric asymmetry remains an open question.

Inconsistent studies exist with regards to maximum occurrence of polar cap patches in the Southern Hemisphere. Coley and Heelis (1998) and Spicher et al. (2017) reported maximum occurrence in local winter, which is the same as in Northern Hemisphere (i.e., maximum in local winter). In contrast, Noja et al (2013) reported minimum occurrence in local winter. This inconsistency indicates that TOIs and/or patches do not always occur simultaneously or have substantial asymmetry between the two hemispheres. Further investigation will be needed in order to understand the UT and/or longitudinal dependence of ionospheric SED plume hemispheric asymmetry, specifically an investigation with more recent data that mitigate the longitudinal inhomogeneity of the GPS receiver coverage.

5.3. What process determines activity dependence of plumes?

The comparison of plumes between 2013 and 2015 in Figures 4 through 8 show that the plume peak density is smaller for the 2015 stronger storm in both the ionosphere and plasmasphere. Furthermore, the plasmaspheric drainage plume location is shifted more toward noon for the stronger storm. Our results are qualitatively consistent with those from the Dynamic Global Core Plasma Model (DGCPM) (e.g., Ober et al., 1997) in which the peak plume densities at L=6.6 were compared for different levels of Kp from 3 to 7 (Borovsky et al., 2014, Figure 12), where the peak plume density is higher for Kp=3 (purple curve). Figure 8 is consistent with Figure 13 of Borovsky et al. 2014 showing that the plume location is shifted more toward noon for the stronger storm. When magnetospheric convection decreases, plumes tend to corotate with the earth because corotation dominates over convection. While the plume MLT locations remain constant in the DGCPM simulation results, the IPE plumes gradually start corrotating with the Earth and shift toward the dusk MLT sector as the geomagnetic activity decreases.

Indeed, our results are also consistent with the statistical analysis of the MPA flux for 6 months from Sep 2015 to Feb 2016 (Denton et al., 2019). In contrast, at magnetopause crossings, however, Walsh et al. (2013) reported that the plume density is positively corelated with geomagnetic activity (PC index) based on the statistical analysis of the cold plasma density observed by THEMIS. On the other hand, in the ionosphere, where larger superstorms tend to show higher plume peak density (e.g., Halloween storm, 2003-10-30), plume peak densities appear to depend also on different parameters such as universal time, season, and IMF B_y, according to the comparison of TEC plumes for six superstorms during the solar cycle 23 (e.g., Coster et al., 2006). For example, GPS-TEC observations suggest that spring and fall equinoxes would require smaller storm intensity in generating the same strength of ionospheric SED plumes as those in other seasons (Coster et al., 2016).

763 Intuitively, one would expect that plume density should be higher for larger storms, which is the
764 2015 storm in our study. But it is still not clear why the plume density is smaller for stronger
765 storms. One possible interpretation is that faster convection for stronger storms transports
766 plasmaspheric plume plasma much more quickly to the dayside magnetopause at which point the
767 plasma gets lost, whereas the slower convection for weaker storms has more than enough time to
768 accumulate plasma (preconditioning effect). Another interpretation is that plasmaspheric
769 drainage plumes at L=6.6 tend to be more distant from the plasmapause location as the
770 plasmapause location gets closer to the Earth for stronger storms. The time history of the
771 magnetospheric system itself, and the conditions existing at the storm onset (i.e., preconditioning
772 effect), also likely play a role.
773 In contrast, in the ionosphere, more extended convection is expected to access higher density
774 produced by solar EUV at lower latitude, as the polar cap extends more equatorward for stronger
775 storms. Furthermore, the role of the contribution of lower latitude plasma source should also be
776 taken into consideration due to the super fountain effect caused by penetration electric fields
777 (e.g., Tsurutani et al., 2004; Mannucci et al., 2005; Lin et al., 2005; Balan et al., 2009).
778 Therefore, one would expect higher SED plume peak density for stronger storms. On the other
779 hand, Figures 4 and 5 show that the ionospheric trough is deeper and expanded more
780 equatorward in 2015 because of faster recombination. Frictional heating between neutral and
781 ionized particles increases ion temperature, resulting in faster O^+ recombination and the
782 subsequent reduction of plasma density (e.g., Schunk et al., 1976). Faster transport due to the
783 stronger convection flow may also play a role in deepening the trough in 2015. As a
784 consequence, the convection would end up plowing a lesser amount of plasma, accumulating a
785 smaller amount of plasma to form a plume (i.e., preconditioning effect).
786 Figure 8 shows that plume location at L=6.6 shifts toward noon for stronger storms, which is
787 consistent with the statistical analysis of the MPA data (Denton et al., 2019). However, in the
788 ionosphere, Foster et al. (1993) reported that the latitude of the SED decreased with increasing
789 local time and with increasing level of storm activity (Kp index). Could this discrepancy be
790 attributed to the difference of the latitude (L value) between MPA at L=6.6 vs. Millstone Hill at
791 L=3? It is also perplexing as to why plumes in the plasmasphere appear to behave differently
792 from those in the ionosphere.
793 The different responses of plumes between the plasmasphere and ionosphere could perhaps be
794 explained by the different underlying processes at work between the plasmasphere and
795 ionosphere. The plasmasphere is mainly controlled by transport (perpendicular **E×B** and parallel)
796 and loss at the dayside magnetopause crossings, while the ionospheric processes are more
797 complicated: transport, solar EUV, auroral precipitation. In addition, ionospheric plasma is
798 strongly coupled to neutral species, e.g., neutral wind, temperature, composition. For example, in
799 Figure 4a, the ionospheric SED plume in GPS-TEC in 2013 was transported well beyond the
800 magnetic pole toward the night side. The corresponding plasmaspheric drainage plume would
801 not have been observed to be transported from the dayside magnetopause crossing to the
802 nightside, because plasma gets lost at the magnetopause crossing. Further investigation will be
803 needed in order to understand the different responses between the plasmasphere and ionosphere
804 and how that understanding could help us finally unravel where the cold, dense plume plasma
805 originates from.
806
807 **5.4. Unsolved Questions:**

There are several fundamental questions on plumes that remain unsolved. What physical processes are responsible for the maintenance of long-lived drainage plumes? Henderson et al. (2018) suggested that a SAPS-associated shear-flow ballooning type of instability operating at the plasmapause could explosively disrupt the plasmapause. This would place high density plasma onto open drift paths and a recurrence of such events during large storms could be responsible for feeding long-lived drainage plumes. What is the relative importance of transporting cold plasma population at the dayside magnetopause between ion outflow at high latitude and plasmaspheric plumes? What is the fate of draining plasmaspheric material at the magnetopause? Borovsky et al. (2014) performed several numerical experiments using a global MHD model and demonstrated that plasmaspheric cold, dense material does indeed participate in the dayside reconnection and reduce the reconnection rates by lowering the Alfvèn velocity. Walsh et al. (2013) showed that the reconnection jet speeds for magnetopause crossings with plumes are lower than those without plumes. Their results suggest that the presence of a plume lowers the Alfvèn speed significantly and potentially the dimensionless reconnection rate. Furthermore, a reduction in ion temperature introduces a new length scale for diffusion regions, resulting in a decrease of the hall physics of a magnetopause magnetic reconnection separatrix layer based on the Magnetospheric Multiscale spacecraft (MMS) observations (e.g., André et al., 2016). But does plasmaspheric material always participate in the dayside reconnection? If not always, exactly under what conditions do plasmaspheric plumes actually participate in the dayside reconnection? Where does the plasmaspheric material go after participating in the reconnection? Does the plasmaspheric material convect on open field lines through the polar cap? Or does the material become captured into the low-latitude boundary layer and then convect on closed field lines around the flanks of the magnetosphere?

5.5. Conclusions

For the purpose of understanding "where does the cold, dense plasma originate from?," we compared the plumes in the ionosphere, plasmasphere and magnetosphere for the two famous St. Patrick's Day storms in 2013 and 2015. The plumes are colocated in the plasmasphere, and ionosphere for both storms. For 2015, simultaneously, the plumes are observed, being transported to the dayside magnetopause (while in 2013 no direct observations were available). The conjugacy of ionospheric SED plumes between the two hemispheres was studied in 2013. The plumes are magnetically conjugate feature, but the structure and magnitude appear to be different.

The plumes' peak density is larger for 2013 in bother ionosphere and plasmasphere. The plasmaspheric plume is shifted toward the noon in 2015: local time of the peak density decreases with increasing level of storm activity as measured by the Kp index. Our results suggest that plasmaspheric drainage plumes were created by the enhanced convective transport toward the sun of plasma that was peeled off from the outer part of the plasmasphere, whereas the ionospheric SED plume plasma came from the density enhancement generated in the dayside subauroral ionosphere. These plumes happened to be observed near the same closed field lines at the peak of the geomagnetic activity because the motion of the cold plasma in the ionosphere and plasmasphere is connected through the ExB drift. Our results are still inconclusive with regards to colocation, conjugacy, and activity dependence because the comparison was made only two cases. Why plumes appear to respond differently between the ionosphere, plasmasphere, and magnetosphere is still an open question. We will need to identify and distinguish physical mechanisms that control plume formation and colocation in a more systematic study. Our results

suggest that more plasmaspheric material is transported toward the magnetopause for weaker magnetic activities toward the dusk MLT sector. In contrast, for stronger activities, more plasmaspheric material that is transported near the noon MLT sector is likely to participate in the dayside magnetic reconnection. It makes us ponder whether storm time convection is connected to regulation of the reconnection rate by bringing plasmaspheric materials to the dayside magnetopause.

Appendix A: IPE Model Further Details

A1. IPE Model Grid

In order to make three-dimensional, global coverage, the IPE simulations in this study use a total of 7,440 flux tubes with 93 in latitude and 80 in longitude directions. The values were chosen to satisfy the certain spatial resolution in terms of altitude and latitude. In this study, the horizontal (latitude and longitude) spatial resolution is sufficient enough to resolve the dynamic evolution of the SED plume/TOI plumes. The longitudinal resolution is 4.5º, while the latitudinal resolution is variable with an average latitudinal resolution of approximately 0.34º. The spatial resolution of the radial direction in the plasmasphere varies from 0.05 R_E (L=1.5) to 0.46 R_E (L=5). The latitude of the most poleward flux tube is 88.2°. No altitude boundary is necessary because all the flux tubes are closed, which provides an advantage of coupling ionosphere and plasmasphere self-consistently. The integration of the model equation calculation is carried out along all the closed field lines in the IPE model, in order to avoid the potential artificial discontinuity created by the boundary conditions. The arc length between two grid points along the magnetic grid has been designed to be less than the plasma scale height for each altitude region. The number of grid points along a field line ranges from 11 near the equator to 1115 at the highest latitude. The parallel solver has been stable in general, regardless of a specified grid spacing (Note that the original number of grid points in FLIP is 400). The grid spacing along a field line is defined by variable height increment as follows:

$$\boldsymbol{dht} = \begin{cases} \boldsymbol{2km}:, & \boldsymbol{ht < 150km} \\ \boldsymbol{10km}:, & \boldsymbol{ht < 600km} \\ \boldsymbol{20km}:, & \boldsymbol{ht < 3000km} \\ \boldsymbol{2000km}:, & \boldsymbol{ht < 10000km} \\ \boldsymbol{5000km}:, & \boldsymbol{ht \geq 10000km} \end{cases}$$

qA at each grid point is evaluated using Equation (6) above, while the arc length along field lines, sA, is defined using Equation (4) above.

A2: IPE Model Parallelization

The original FLIP one-dimensional solver is very efficient and can run on a conventional laptop in a serial mode. After adding 93 × 80 flux tubes and perpendicular transport, we soon discovered that 3-D IPE was computationally very expensive, and thus IPE simulations run very slow when running in a serial mode. To improve computational efficiency, the IPE model has been parallelized by using the Message Passing Interface (MPI) by using a library called the Scalable Modeling System (SMS) (Govett et al., 2003). The SMS pre-processing script automatically generates an MPI code when building the executable by using a pre-processing script. The advantage of using SMS is that one needs to maintain only a single version of a

source code for either serial or parallel usage, because the SMS directives are ignored when compiling for a serial version. Furthermore, SMS gives flexibility in decomposing the model domain in both latitude and longitude directions: the processor layout is requested at run-time. In this study, a total of 464 processors (58 in latitude and 8 longitude) were used.

A3: IPE Model Minor Ion Chemistry

The FLIP model incorporates the basic chemical scheme that was developed originally from the Atmospheric Explorer (AE) mission but has been continually updated as more information becomes available. The minor ion densities are obtained assuming the local chemical equilibrium for NO^+, O_2^+, N_2^+, $O^+(^2P)$, and $O^+(^2D)$ below 500 km altitude in each hemisphere. The minor ions contribute to the ionization below 400 km. The densities of minor neutral species NO, $O(^1D)$, $N(^2D)$, $N(^4S)$ are also obtained by solving the equations of continuity and momentum in each hemisphere separately. Richards (2011a) gives a summary of the ion chemistry scheme. A complete list of reaction rates is given in Richards (2011b). The ion chemistry in FLIP has been validated against Atmosphere Explorer satellite data Richards (2011a). The original FLIP model also solves for the first five excited states of vibrationally excited N_2 by solving continuity and momentum equations in each hemisphere because the $O^+ + N_2$ loss rate is greatly enhanced for vibrational levels greater than one. It is also an important channel for neutral gas heating. However, the current version of the IPE model has not included the calculation purely because the computation can become expensive in the global model. Instead, the reaction rate has been modified to simulate the effect of vibrational excitation as described by Richards et al. (2018). The model also calculates the thermosphere neutral heating rate from exothermic reactions. The exothermicities of the various reactions is given in Torr (1980a, b). In addition to exothermic reactions, FLIP includes the translational energy from the dissociation of molecular nitrogen (Richards, 2012).

Acknowledgments, Samples, and Data

The authors would like to acknowledge valuable discussions with Joe Borovsky, Dan Welling, Phil Erickson in preparing the manuscript, and acknowledge support from Art Richmond, Astrid Maute, Tzu-Wei Fang in implementing the Apex coordinates in the IPE model. We acknowledge use of NASA OMNI website (omniweb.gsfc.nasa.gov) for the solar wind parameters and NASA/GSFC's Space Physics Data Facility's CDA Web for THEMIS data. The TEC data are available at http://cedar.openmadrigal.org/ . Daily values of F10.7 were obtained from the NOAA NGDC ftp website. This work was supported by NASA grants (NNX16AB83G, NNX15AI91G, 80NSSC17K0720, 80NSSC17K0718, 80NSSC19K0084, 80NSSC19K0277, 80NSSC18K0657), NSF grants (AGS-1452298, AGS-1552248, AGS-1907698), and AFOSR FA9550-18-1-0483. We thank support from the CEDAR workshop "Grand Challenge: Multi scale I-T system dynamics" and the previous “Grand challenge: Storms and Substorms Without Border”. GPS TEC data products and access through the Madrigal distributed data system are provided to the community by the Massachusetts Institute of Technology under support from US National Science Foundation grant AGS-1242204. Data for the TEC processing is provided from the following organizations: UNAVCO, Scripps Orbit and Permanent Array Center, Institut Geographique National, France, International GNSS Service, The Crustal Dynamics Data Information System (CDDIS), National Geodetic Survey, Instituto Brasileiro de Geografia e Estatística, RAMSAC CORS of Instituto Geográfico Nacional de la República Argentina,

939 Arecibo Observatory, Low-Latitude Ionospheric Sensor Network (LISN), Topcon Positioning
940 Systems, Inc., Canadian High Arctic Ionospheric Network, Institute of Geology and Geophysics,
941 Chinese Academy of Sciences, China Meteorology Administration, Centro di Ricerche
942 Sismologiche, Système d'Observation du Niveau des Eaux Littorales (SONEL), RENAG :
943 REseau NAtional GPS permanent, GeoNet - the official source of geological hazard information
944 for New Zealand, GNSS Reference Networks, Finnish Meteorological Institute, SWEPOS -
945 Sweden, Hartebeesthoek Radio Astronomy Observatory, Crustal Dynamics Data Information
946 System (CDDIS), Astronomical Institute of the University of Bern, TrigNet Web Application,
947 South Africa, Australian Space Weather Services, RETE INTEGRATA NAZIONALE GPS,
948 Estonian Land Board, and Virginia Tech Center for Space Science and Engineering Research.
949 Data used in the study are available in the CU Scholar repository
950 (https://scholar.colorado.edu/dashboard).

951 **References**

952

953 Akmaev, R. A., and H.-M. H. Juang (2008), Using enthalpy as a prognostic variable in
954 atmospheric modelling with variable composition, *Q. J. R. Meteorol. Soc*., 134(637), 2193–2197,
955 doi:10.1002/qj.345.
956
957 Akmaev, R. A., T. J. Fuller-Rowell, F. Wu, J. M. Forbes, X. Zhang, A. F. Anghel, M. D. Iredell,
958 S. Moorthi, and H.-M. Juang (2008), Tidal variability in the lower thermosphere: Comparison of
959 Whole Atmosphere Model (WAM) simulations with observations from TIMED, *Geophys. Res.*
960 *Lett.,* 35, L03810, doi:10.1029/2007GL032584
961

962 André, M., et al. (2016), Magnetic reconnection and modification of the Hall physics due to cold
963 ions at the magnetopause, Geophys. Res. Lett., 43, 6705–6712, doi:10.1002/2016GL069665.

964 Auster, H. U., et al. (2008), The THEMIS fluxgate magnetometer, Space Sci. Rev., 141, 235–
965 264.
966

967 Bailey, G.J., Balan, N., (1996). A low latitude ionosphere/Plasmasphere model. In: Schunk,
968 R.W. (Ed.), STEP Hand Book. Utah State University, Logan, pp. 173–206.

969
970 Bame, S. J., D. J. McComas, M. F. Thomsen, B. L. Barraclough, R. C. Elphic, J. P. Glore, J. T.
971 Gosling, J. C. Chavez, E. P. Evans, and F. J. Wymer (1993), Magnetospheric plasma analyzer for
972 spacecraft with constrained resources, Rev. Sci. Instrum., 64, 1026.
973
974 Balan, N., K. Shiokawa, Y. Otsuka, S. Watanabe, and G. J. Bailey (2009), Super plasma fountain
975 and equatorial ionization anomaly during penetration electric field, *J. Geophys. Res*., 114,
976 A03310, doi:10.1029/2008JA013768.
977
978 Banks, P. (1966), Collision frequency and energy transfer: Ions, Planet. Space Sci., 14, 1105—
979 1122, doi:10.1016/0032-0633(66)90025-0

Bonnell, J. W., F. S. Mozer, G. T. Delory, A. J. Hull, R. E. Ergun, C. M. Cully, V. Angelopoulos, and P. R. Harvey (2008), The Electric Field Instrument (EFI) for THEMIS, Space Sci. Rev., 141, 303–341, doi:10.1007/s11214-008-9469-2.

Borovsky, J. E., and M. H. Denton (2006), The effect of plasmaspheric drainage plumes on solar- wind/magnetosphere coupling, Geophys. Res. Lett., 33, L20101.

Borovsky, J. E., and M. H. Denton (2008), A statistical look at plasmaspheric drainage plumes, J. Geophys. Res., 113, A09221, doi:10.1029/2007JA012994.

Borovsky, J. E., M. F. Thomsen, and D. J. McComas (1997), The super- dense plasma sheet: Plasmaspheric origin, solar-wind origin, or iono- spheric origin?, J. Geophys. Res., 102, 22,089.

Borovsky, J. E., M. F. Thomsen, D. J. McComas, T. E. Cayton, and D. J. Knipp (1998), Magnetospheric dynamics and mass flow during the November 1993 storm, J. Geophys. Res., 103, 26,373.

Borovsky, J. E., M. Hesse, J. Birn, M.M. Kuznetsova, (2008) What determines the reconnection rate at the dayside magnetosphere?, J. Geophys. Res. Space Physics, 113, doi:10.1029/2007JA012645.

Borovsky, J. E., M. H. Denton, R. E. Denton, V. K. Jordanova, and J. Krall (2013), Estimating the effects of ionospheric plasma on solar-wind/magnetosphere coupling via mass loading of dayside reconnection: Ion-plasma-sheet oxygen, plasmaspheric drainage plumes, and the plasma cloak, J. Geophys. Res. Space Physics, 118, 5695–5719.

Borovsky, J. E., D. T. Welling, M. F. Thomsen, and M. H. Denton (2014), Long-lived plasmaspheric drainage plumes: Where does the plasma come from?, J. Geophys. Res. Space Physics, 119, 6496–6520, doi:10.1002/2014JA020228.

Brace, L. H., H. G. Mayr, and B. M. Reddy (1968), The early effects of increasing solar activity upon the temperature and density of the 1000-kilometer ionosphere, J. Geophys. Res., 73, 1607.

Burnside, R. G., C. A. Tepley, and V. B. Wickwar (1987), The O-O colli- sion cross-section: can it be inferred from aeronomical measurements?, Ann. Geophys., 5, 343–350.

Carpenter, D. L. and Lemaire, J.: The plasmasphere boundary layer (2004), *Ann. Geophys*., 22, 4291–4298, doi:10.5194/angeo-22–4291-2004.

Carpenter, D. L., & Park, C. G. (1973). What ionospheric workers should know about the plasmapause-plasmasphere. Reviews of Geophysics, 11(1), 133–154. https://doi.org/10.1029/RG011i001p00133

Carpenter, D. L., B. L. Giles, C. R. Chappell, P. M. E. Decreau, R. R. Anderson, A. M. Persoon, A. J. Smith, Y. Corcuff, and P. Canu (1993), Plasmasphere dynamics in the duskside bulge region: A new look at an old topic, *J. Geophys. Res*., 98, 19243, doi:10.1029/93JA00922.

Cassak P. A., and M. A. Shay (2007), Scaling of asymmetric magnetic reconnection: General theory and collisional simulations, Phys. Plasmas, 14, 102114, doi:1070-664X/2007/14(10)/102114/11.

Cassak, P. A., and S. A. Fuselier (2016), Reconnection at Earth's dayside magnetopause, in Magnetic Reconnection, edited by W. Gonzalez and E. Parker, Astrophys. and Space Sci Library, 427, Springer, Switzerland, doi: 10.1007/978-3-319-26432-5, p. 213-276.

Chappell, C. R., K. K. Harris, and G.W. Sharp (1971), The dayside plasmasphere, *J. Geophys. Res*., 76, 7632, https://doi.org/10.1029/JA076i031p07632

Coley, W. R., and R. A. Heelis (1998), Seasonal and universal time distribution of patches in the northern and southern polar caps, *J. Geophys. Res*., 103(A12), 29229–29237, doi:10.1029/1998JA900005

Coster, A. J., M. J. Colerico, J. C. Foster, W. Rideout, and F. Rich (2007), Longitude sector comparisons of storm enhanced density, Geophys. Res. Lett., 34, L18105, doi:10.1029/2007GL030682.

Coster, A. J., P. J. Erickson, J. C. Foster, E. G. Thomas, J. M. Ruohoniemi, and J. Baker (2016), Solar Cycle 24 Observations of Storm-Enhanced Density and the Tongue of Ionization. In T. Fuller-Rowell, E. Yizengaw, P. H. Doherty, S. Basu (Eds.), Ionospheric Space Weather: Longitude Dependence and Lower Atmosphere Forcing, Geophysical Monograph Series. (Vol. 220, pp. 71–84). Washington, DC, American Geophysical Union.

Craven, P. D., D. L. Gallagher, and R. H. Comfort (1997), Relative concentration of He+ in the inner magnetosphere as observed by the DE 1 retarding ion mass spectrometer, J. Geophys. Res., 102, 2279.

Denton, M. H., M. F. Thomsen, H. Korth, S. Lynch, J. C. Zhang, and M. W. Liemohn (2005), Bulk plasma properties at geosynchronous orbit, J. Geophys. Res., 110, A07223, doi:10.1029/2004JA010861.

1054 Denton, M. H., Henderson, M. G., Maruyama, N., & Fuselier, S. A. (2019). The cold ion
1055 population at geosynchronous orbit and transport to the dayside magnetopause: September 2015
1056 to February 2016. Journal of Geophysical Research: Space Physics, 124. https://doi.org/10.1029/
1057 2019JA026973.
1058
1059 Doering, J. P., and Goembel, L. (1991), Absolute differential and integral electron excitation
1060 cross sections for atomic nitrogen: 1. The $^4S^o \rightarrow 3s^4P$ (λ1200 Å) transition from 30 to 100 eV, J.
1061 Geophys. Res., *96*(A9), 16021–16024, doi:10.1029/91JA01462.
1062
1063 Elphic, R. C., L. A. Weiss, M. F. Thomsen, D. J. McComas, and M. B. Moldwin (1996),
1064 Evolution of plasmaspheric ions at geosynchronous orbit during times of high geomagnetic
1065 activity, Geophys. Res. Lett., 23, 2189–2192.
1066
1067 Elphic, R. C., M. F. Thomsen, and J. E. Borovsky (1997), The fate of the outer plasmasphere,
1068 Geophys. Res. Lett., 24, 365.
1069
1070 Evans, D. S., Global Statistical Patterns of Auroral Phenomena, in Proceedings of the
1071 Symposium on Quantitative Modeling of Magnetospheric-Ionospheric Coupling Processes, 325,
1072 Kyoto, 1987.
1073
1074 Ferdousi, B., Nishimura, Y., Maruyama, N., and Lyons, L.R. (2019) Subauroral neutral wind
1075 driving and its feedback to SAPS during the March 17, 2013 geomagnetic storm, J. Geophys.
1076 Res.: Space Physics, doi: 10.1029/2018JA026193
1077
1078 Foster, J. C. (1993), Storm-time plasma transport at middle and high latitudes, J. Geophys. Res.,
1079 98, 1675–1689; doi:10.1029/ 92JA02032.
1080
1081 Foster, J. C., and W. Rideout (2007), Storm enhanced density: Magnetic conjugacy effects, Ann.
1082 Geophys., 25, 1791–1799; doi:10.5194/angeo-25-1791-2007.
1083
1084 Foster, J. C., A. J. Coster, P. J. Erickson, J. Goldstein, and F. J. Rich (2002), Ionospheric
1085 signatures of plasmaspheric tails, *Geophys. Res. Lett*., 29(13), 1623, doi:10.1029/2002GL015067
1086
1087 Foster, J. C., A. J. Coster, P. J. Erickson, J. M. Holt, F. D. Lind, W. Rideout, M. McCready, et al.
1088 (2005), Multiradar observations of the polar tongue of ionization, *J. Geophys. Res*., 110,
1089 A09S31, doi:10.1029/2004JA010928
1090
1091 Foster, J. C., W. Rideout, B. Sandel, W. T. Forrester, and F. J. Rich (2007), On the relationship
1092 of SAPS to storm enhanced density, *J. Atmos. Space Terr. Phys*., 69, 303–313.
1093
1094 Foster, J. C., P. J. Erickson, A. J. Coster, S. Thaller, J. Tao, J. R. Wygant, and J. Bonnell (2014),
1095 Stormtime observations of plasmasphere erosion flux in the magnetosphere and ionosphere,
1096 Geophys. Res. Lett., 41, 762–768, doi:10.1002/2013GL059124
1097

1098 Fuller-Rowell, T. J., & Evans, D. S. (1987). Height-integrated Pedersen and Hall conductivity
1099 patterns inferred from the TIROS-NOAA satellite data. Journal of Geophysical Research,
1100 92(A7), 7606–7618. https://doi.org/10.1029/JA092iA07p07606

1101

1102 Fuller-Rowell, T., D. Rees, S. Quegan, R. Moffett, and G. Bailey (1987), Interactions between
1103 neutral thermospheric composition and the polar ionosphere using a coupled ionosphere
1104 thermosphere model, J. Geophys. Res., 92(A7), 7744–7748, doi:10.1029/JA092iA07p07744.

1105 Fuller-Rowell, T. J., D. Rees, S. Quegan, R. J. Moffett, M. V. Codrescu, and G. H. Millward
1106 (1996), A coupled thermosphere-ionosphere model (CTIM), in STEP Handbook of Ionospheric
1107 Models, edited by R. W. Schunk, pp. 217–238, Utah State Univ, Logan.

1108
1109 Fuller-Rowell, T. J., R. A, Akmaev, F. Wu, A. Anghel, N. Maruyama, D. N. Anderson, M. V.
1110 Codrescu, M. Iredell, S. Moorthi, H.-M. Juang, Y.-T. Hou, and G. Millward, (2008). Impact of
1111 terrestrial weather on the upper atmosphere, Geophys. Res. Lett., 35, L09808,
1112 doi:10.1029/2007GL032911.
1113

1114 Fuller-Rowell, T. J., A. D. Richmond, and N. Maruyama (2008), Global modeling of storm-time
1115 thermospheric dynamics and electrodynamics, in Midlatitude Ionospheric Dynamics and
1116 Disturbances, AGU Geophys. Monograph Ser., edited by P. M., Kintner, Jr., A. J. Coster, T. J.
1117 Fuller-Rowell, A. J. Mannucci, M. Mendillo, and R. Heelis, vol. 181, pp. 187–200, AGU,
1118 Washington, DC, doi:10.1029/181GM18.

1119 Fuselier, S. A., et al. (2016), Magnetospheric ion influence on magnetic reconnection at the
1120 duskside magnetopause, Geophys. Res. Lett.,43,1435–1442, doi:10.1002/2015GL067358
1121
1122 Fuselier, S.A., J. L. Burch, J. Mukherjee, K. J. Genestreti, S. K. Vines, R. Gomez, J. Goldstein,
1123 K. J. Trattner, S. M. Petrinec, B. Lavraud and R. J. Strangeway, Magnetospheric ion influence at
1124 the dayside magnetopause, (2017) Journal of Geophysical Research: Space Physics, 122, 8,
1125 (8617-8631), (2017).
1126
1127 Fuselier, S.A., K. J. Trattner, S. M. Petrinec, M. H. Denton, S. Toledo-Redondo, M. André, N.
1128 Aunai, C. R. Chappell, A. Glocer, S. E. Haaland, M. Hesse, L. M. Kistler, B. Lavraud, W. Li, T.
1129 E. Moore, D. Graham, L. Alm, P. Tenfjord, J. Dargent, S. K. Vines, K. Nykyri, J. L. Burch,R. J.
1130 Strangeway, (2019) Mass Loading the Earth's Dayside Magnetopause Boundary Layer and Its
1131 Effect on Magnetic Reconnection, Journal of Geophysical Research: Space Physics,
1132 https://doi.org/10.1029/2019GL082384.
1133
1134 Goldstein, J. (2006). Plasmasphere response: Tutorial and review of recent imaging results.
1135 Space Science Reviews, 124(1-4), 203–216. https://doi.org/10.1007/s11214-006-9105-y
1136

Govett, M. L. Hart, T. Henderson, J. Middlecoff and D. Schaffer (2003). The Scalable Modeling System: Directive-based code parallelization for distributed and shared memory computers, Parallel Computing, 29(8), 995–1020, doi: https://doi.org/10.1016/S0167-8191(03)00084-X.

Guerrero, A., Palacios, J., Rodríguez-Bouza, M., Rodríguez-Bilbao, I., Aran, A., Cid, C., ...Cerrato, Y. (2017). Storm and substorm causes and effects at midlatitude location for the St. Patrick's 2013 and 2015 events. Journal of Geophysical Research: Space Physics, 122, 9994–10,011. https://doi.org/10.1002/2017JA024224.

Hedin, A. E., Fleming, E. L., Manson, A. H., Schmidlin, F. J., Avery, S. K., Clark, R. R., et al. (1996). Empirical wind model for the upper, middle and lower atmosphere. Journal of Atmosphere and Terrestrial Physics, 58(13), 1421–1447. https://doi.org/10.1016/0021-9169(95)00122-0

Heelis, R. A., J. J. Sojka, M. David, and R. W. Schunk (2009), Storm time density enhancements in the middle-latitude dayside ionosphere, J.Geophys.Res., 114, A03315; doi:10.1029/2008JA013690.

Henderson, M. G., Morley, S. K., & Kepko, L. E. (2018). SAPS-associated explosive brightening on the duskside: A new type of onset-like disturbance. Journal of Geophysical Research: Space Physics, 123, 197– 210. https://doi.org/10.1002/2017JA024472

Huba, J. D., G. Joyce, and J. A. Fedder (2000a), SAMI2 is another model of the ionosphere (SAMI2): A new low-latitude ionosphere model, J. Geophys. Res., 105(A10), 23,035.

Jones, R. A., and M. H. Rees, (1973) Time dependent studies of the aurora, 1, Ion density and composition, Planet. Space Sci., 21, 537.

Jordanova, V. K. (2006), Modeling the behavior of corotating interaction region driven storms in comparison with coronal mass ejection driven storms, in Recurrent Magnetic Storms, edited by B. Tsurutani et al., p. 77, AGU, Washington, D. C.

Kendall, P. C. (1962), Geomagnetic control of diffusion in the F2-region of the ionosphere—I. The form of the diffusion operator, J. Atmos. Terr. Phys., 24, 805–811, doi:10.1016/0021-9169(62)90201-5.

Knudsen, W. C. (1974), Magnetospheric convection and the high-latitude F2 ionosphere, J. Geophys. Res., 79(7), 1046–1055, doi:10.1029/JA079i007p01046

Krall, J., J.D. Huba, and J.E. Borovsky (2018), SAMI3 simulations of a persistent plasmasphere plume, Geophys. Res. Lett., https://doi.org/10.1002/2017GL076448.

1178 Lambour, R. L., L. A. Weiss, R. C. Elphic, and M. F. Thomsen (1997), Global modeling of the
1179 plasmasphere following storm sudden commencements, J. Geophys. Res., 102, 24,351.
1180

1181 Lemaire, J. F., and K. I. Gringauz (1998), The Earth's Plasmasphere, Cambridge Univ. Press,
1182 New York.

1183
1184 Liemohn, M.W., A. J. Ridley, J. U. Kozyra, D. L. Gallagher, M. F. Thomsen, M. G. Henderson,
1185 M. H. Denton, P. C. Brandt, and J. Goldstein (2006), Analyzing electric field morphology
1186 through data-model comparisons of the Geospace Environment Modeling Inner
1187 Magnetosphere/Storm Assessment Challenge events, J. Geophys. Res., 111, A11S11,
1188 doi:10.1029/2006JA011700.
1189
1190 Lin, C. H., A. D. Richmond, R. A. Heelis, G. J. Bailey, G. Lu, J. Y. Liu, H. C. Yeh, and S.-Y. Su
1191 (2005), Theoretical study of the low- and midlatitude ionospheric electron density enhancement
1192 during the October 2003 superstorm: Relative importance of the neutral wind and the electric
1193 field, *J. Geophys. Res*., 110, A12312, doi:10.1029/2005JA011304
1194
1195 Liu, J., W. Wang, A. Burns, X. Yue, S. Zhang, Y. Zhang, and C. Huang (2016a), Profiles of
1196 ionospheric storm-enhanced density during the 17 March 2015 great storm, *J. Geophys. Res*.:
1197 *Space Physics*, 121 727–744, doi:10.1002/2015JA021832
1198
1199 Liu, J., W. Wang, A. Burns, S. C. Solomon, S. Zhang, Y. Zhang, and C. Huang (2016b),Relative
1200 importance of horizontal andvertical transports to the formation ofionospheric storm-enhanced
1201 densityand polar tongue of ionization,J. Geophys. Res. Space Physics,121,8121–8133,
1202 doi:10.1002/2016JA022882
1203
1204 MacDonald, E. A., L. W. Blum, S. P. Gary, M. F. Thomsen, and M. H. Denton (2010), High-
1205 speed stream driven inferences of global wave -distributions at geosynchronous orbit: Relevance
1206 to radiation-belt dynamics, Proc. R. Soc. A, 466, 3351–3362, doi:10.1098/rspa.2010.0076.
1207
1208 Mannucci, A. J., B. T. Tsurutani, B. A. Iijima, A. Komjathy, A. Saito, W. D. Gonzalez, F. L.
1209 Guarnieri, J. U. Kozyra, and R. Skoug (2005), Dayside global ionospheric response to the major
1210 interplanetary events of October 29–30, 2003 ''Halloween Storms,'' *Geophys. Res. Lett*., 32,
1211 L12S02, doi:10.1029/2004GL021467
1212
1213 Maruyama, N., A. D. Richmond, T. J. Fuller-Rowell, M. V. Codrescu, S, Sazykin, F. Toffoletto,
1214 R. W. Spiro, and G. H. Millward (2005), Interaction between direct penetration and disturbance
1215 dynamo electric fields in the storm-time equatorial ionosphere, *Geophys. Res. Lett*.,
1216 doi:10.1029/2005GL023763.
1217
1218 Maruyama, N., S. Sazykin, R. W. Spiro, D. Anderson, A. Anghel, R. A. Wolf, F. Toffoletto, T. J.
1219 Fuller-Rowell, M. V. Codrescu, A. D. Richmond, and G. H. Millward (2007), Modeling storm-
1220 time electrodynamics of the low latitude ionosphere-thermosphere system: Can long lasting

disturbance electric fields be accounted for?, *J. Atmos. Solar Terr. Physics*., 69(10), 1182–1199, doi:10.1016/j.jastp.2006.08.020

Maruyama, N., Fuller-Rowell, T. J., Codrescu, M. V., Anderson, D., Richmond, A. D., Maute, A. et al. (2011), Modeling the storm time electrodynamics. In M. A. Abdu, D. Pancheva, (Eds.), *Aeronomy of the Earth's atmosphere and ionosphere*, *IAGA, Special Sopron Book Series* (Vol. 2, pp. 455–464). Springer, Dordrecht. doi:10.1007/978-94-007-0326-1

Maruyama, N., Sun, Y.-Y., Richards, P. G., Middlecoff, J., Fang, T.-W., Fuller-Rowell, T. J., et al. (2016). A new source of the midlatitude ionospheric peak density structure revealed by a new Ionosphere-Plasmasphere model. Geophysical Research Letters, 43, 2429–2435. https://doi.org/10.1002/2015GL067312

Maruyama, N., P. Li, R. Oehmke, G. Theurich, C. DeLuca, T. J. Fuller-Rowell, T.-W. Fang, P. Richards, M. Fedrizzi, M. Codrescu, W. Yang, R. Akmaev, V. Yudin, H. Wang, M. Iredell, J. Middlecoff, M. Govett, A. Maute, A. D. Richmond, A. Coster, and R. Viereck (2017), Ionospheric weather from the Coupled Whole Atmosphere model (WAM)-Ionosphere-Plasmasphere-Electrodynamics (IPE) model toward NOAA Operational space weather forecasting, 2017 AMS meeting, Seattle, WA, USA.

Maruyama, N. (2020), Chapter 9. Storms and substorms—the new whole system approach and future challenges, in "The Dynamical Ionosphere" edited by Massimo Materassi, Anthea Coster, Susan Skone and Biagio Forte, Elsevier, https://doi.org/10.1016/B978-0-12-814782-5.00009-1.

Maus, S., Macmillan, S., Chernova, T., Choi, S., Dater, D., Golovkov, V., et al. (2005). The 10th-generation international geomagnetic reference field. Geophysical Journal International, 161(16), 561–565. https://doi.org/10.1029/2005EO160006

McComas, D. J., et al., Magnetospheric plasma analyzer: Initial three-spacecraft observation from geosynchronous orbit, J. Geophys. Res., 98, 13,453, 1993.

McFadden, J. P., C.W. Carlson, D. Larson, M. Ludlam, R. Abiad, B. Elliott, P. Turin, M. Marckwordt, and V. Angelopoulos (2008), The THEMIS ESA plasma instrument and in-flight calibration, Space Sci. Rev, 141, 277–302, doi:10.1007/s11214-008-9440-2.

Mendillo, M., M. D. Papagiannis, and J. A. Klobuchar (1970), Ionospheric storms at midlatitudes, *Radio Sci*., 5, 895–898, 10.1029/RS005i006p00895

Millholland, S., N. Maruyama, A. Maute, L. Goncharenko, A. Burns, P. Richards, T.-W. Fang, and T. Fuller-Rowell (2013), Modeling sudden stratospheric warming events using the Ionosphere-Plasmasphere-Electrodynamics (IPE) Model, 2013 Fall meeting, San Francisco, December 8-13.

Millward, G. H., I. C. F. Müller-Wodarg, A. Aylward, T. J. Fuller-Rowell, A. D. Richmond, and R. J. Moffett (2001), An investigation into the influence of tidal forcing on F region equatorial

vertical ion drift using a global ionosphere-thermosphere model with coupled electrodynamics, J. Geophys. Res., 106(A11), 24,733–24,744, doi:10.1029/2000JA000342.

Moen, J. I., K. Oksavik, L. Alfonsi, Y. Dåbakk, V. Romano, and L. Spogli (2013), Space weather challenges of the polar cap ionosphere*, J. Space Weather Space Clim*., 3(A02), doi:10.1051/swsc/2013025.

Nagy, A. F., and P.M. Banks (1970), Photoelectron fluxes in the ionosphere, J. Geophys. Res.,75,6260.

Newberry, I. T., R. H. Comfort, P. G. Richards, and C. R. Chappell (1989), Thermal He^+ in the plasmasphere: Comparison of observation with numerical calculations, J. Geophys. Res., 94, 15,265.

Nishimura, Y., et al. (2013), Structures of dayside whistler-mode waves deduced from conjugate diffuse aurora, J. Geophys. Res. Space Physics, 664–673, doi:10.1029/2012JA018242.

Noja, M., C. Stolle, J. Park, and H. Lühr (2013), Long-term analysis of ionospheric polar patches based on CHAMP TEC data, *Radio Sci*., 48, 289–301, doi:10.1002/rds.20033

Ober, D. M., J. L. Horwitz, and D. L. Gallagher (1997), Formation of density troughs embedded in the outer plasmasphere by subauroral ion drifts, J. Geophys. Res., 102, 14,595–14,602, doi:10.1029/97JA01046.

Obana, Y., Maruyama, N., Shinbori, A., Hashimoto, K. K., Fedrizzi, M., Nosé, M., et al. (2019). Response of the ionosphere-plasmasphere coupling to the September 2017 storm: What erodes the plasmasphere so severely? Space Weather, 17, 861–876. https://doi.org/10.1029/2019SW002168

Ouellette, J. E., Lyon, J. G., Brambles, O. J., Zhang, B., and Lotko, W. (2016), The effects of plasmaspheric plumes on dayside reconnection, *Journal of Geophysical Research: Space* Physics, 121(5), 4111–4118, doi:10.1002/2016JA022597

Picone, J. M., Hedin, A. E., Drob, D. P., & Aikin, A. C. (2002). NRLMSISE-00 empirical model of the atmosphere: Statistical comparisons and scientific issues. Journal of Geophysical Research, 107(A12), 1468. https://doi.org/10.1029/2002JA009430

Pokhotelov, D., Mitchell, C. N., Jayachandran, P. T., MacDougall, J. W., and Denton, M. H. (2009), Ionospheric response to the corotating interaction region–driven geomagnetic storm of October 2002, *J. Geophys. Res*., 114, A12311, doi:10.1029/2009JA014216

Raeder, J., W. D. Cramer, J. Jensen, T. Fuller-Rowell, N. Maruyama, F. Toffoletto, and H. Vo (2016), Sub-Auroral Polarization Streams: A complex interaction between the magnetosphere,

ionosphere, and thermosphere, Journal of Physics Conference Series, 767, 1-10, 2016. 012021, (DOI: 10.1088/1742-6596/767/1/012021).

Rapp, D., and P. Englander-Golden, Total cross sections for ionization and attachment in gases by electron impact I, Positive ionization. J. Chem. Phys., 43, 1464, 1965.

Rees, M. H., (1963) Auroral ionization and excitation by incident energetic electrons, Planet. Space Sci., 11, 1209.

Richards, P.G. (1978) A numerical study of ionosphere-protonosphere coupling, Ph.D. Thesis, La Trobe University, Australia.

Richards, P. G. (2011a), Reexamination of ionospheric photochemistry, J. Geophys. Res., doi:10.1029/2011JA016613

Richards, P. G. (2011b), Reevaluation of thermosphere heating by auroral electrons, Adv. Space Res., doi:10.1016/j.asr.2011.09.004

Richards, P. G. (2012), Re-evaluation of thermosphere heating by Solar EUV and UV radiation, Canadian Journal of Physics, 90(8): 759-767, https://doi.org/10.1139/p11-109

Richards, P. G., and D. G. Torr (1985), On the production of N+ by energetic electrons, J. Geophys. Res., 90, https://doi.org/10.1029/JA090iA10p09917

Richards, P. G., and D. G. Torr (1990), Auroral modeling of the 3371 A emission rate: Dependence on characteristic electron energy, J. Geophys. Res., 95, 10,337–10,344.

Richards, P. G., Fennelly, J. A., & Torr, D. G. (1994). EUVAC: A solar EUV flux model for aeronomic calculations. Journal of Geophysical Research, 99(A5), 8981–8992. https://doi.org/10.1029/94JA00518

Richards, P. G., T. N. Woods, and W. K. Peterson (2006), HEUVAC: A new high resolution solar EUV proxy model, Adv. Space Res., 37(2), 315–322, doi:10.1016/j.asr.2005.06.031.

Richards, P. G., Meier, R. R., & Wilkinson, P. J. (2010). On the consistency of satellite measurements of thermospheric composition and solar EUV irradiance with Australian ionosonde electron density data. Journal of Geophysical Research, 115, A10309. https://doi.org/10.1029/2010JA015368.

Richards, P.G., R. R. Meier, Shihping Chen, P. Dandenault (2018), Investigation of the causes of the longitudinal and solar cycle variation of the electron density in the Bering Sea and Weddell Sea anomalies, J. Geophys. Res. Space Physics, 122, doi: 10.1029/2018JA025413.

Richmond, A. D. (1995). Ionospheric electrodynamics using magnetic apex coordinates. Journal of Geomagnetism and Geoelectricity, 47(2), 191–212. https://doi.org/10.5636/jgg.47.191.

Richmond, A. D., and A. Maute (2014), Ionospheric electrodynamics modeling, in Modeling the Ionosphere-Thermosphere, Geophys. Monogr. Ser., vol. 201, edited by J. D. Huba et al., AGU, Washington, D. C., doi:10.1002/9781118704417.

Rideout, W., and A. Coster (2006), Automated GPS processing for global total electron content data, GPS Solut.; doi: 10.1007/s10291-006-0029-5.

Sandel, B. R., and M. H. Denton (2007), Global view of refilling of the plasmasphere, Geophys. Res. Lett., 34, L17102, doi:10.1029/2007GL030669

Sato, T. (1959), Morphology of ionospheric F2 disturbances in the polar regions, Rept. Ionosphere Space Res. Japan, 13, 91--104

Sato, T., and G. F. Rourke (1964), F-region enhancements in the Antarctic, J. Geophys. Res., 69(21), 4591–4607, doi:10.1029/JZ069i021p04591

Scherliess, L., and B. G. Fejer (1999), Radar and satellite global equatorial F region vertical drift model, J. Geophys. Res., 104(A4), 6829–6842, doi:10.1029/1999JA900025.

Schunk, R. W., Banks, P. M., and Raitt, W. J. (1976), Effects of electric fields and other processes upon the nighttime high-latitude *F* layer, *J. Geophys. Res*., 81(19), 3271–3282, doi:10.1029/JA081i019p03271

Sojka, J. J., M. David, R. W. Schunk, and R. A. Heelis (2012), A modeling study of the longitudinal dependence of storm time midlatitude dayside total electron content enhancements, *J. Geophys. Res*., 117, A02315, doi:10.1029/2011JA017000

Spicher, A., L. B. N. Clausen, W. J. Miloch, V. Lofstad, Y. Jin, and J. I. Moen (2017), Interhemispheric study of polar cap patch occurrence based on Swarm in situ data, *J. Geophys. Res.: Space Physics*, 122, 3837–3851, doi:10.1002/2016JA023750

Staniforth, A., and J. Côté (1991), Semi-Lagrangian integration schemes for atmospheric models—A review, Mon. Weather Rev., 119, 2206–2223, doi:10.1175/1520-0493(1991)119<2206:SLISFA>2.0.CO;2.

Su, Y.-J., J. E. Borovsky, M. F. Thomsen, R. C. Elphic, and D. J. McComas (2000), Plasmaspheric material at the reconnecting magnetopause, J. Geophys. Res., 105, 7591.

1387 Su, Y.-J., M. F. Thomsen, J. E. Borovsky, and J. C. Foster (2001), A linkage between polar
1388 patches and plasmaspheric drainage plumes, Geophys. Res. Lett., 28, 111,
1389 doi:10.1029/2000GL012042

1390 Sun, Y.-Y., Matsuo, T., Maruyama, N., & Liu, J.-Y. (2015). Field-aligned neutral wind bias
1391 correction scheme for global ionospheric modeling at midlatitudes by assimilating FORMOSAT-
1392 3/COSMIC hmF2 data under geomagnetically quiet conditions. Journal of Geophysical
1393 Research: Space Physics, 120, 3130–3149. https://doi.org/10.1002/2014JA020768

1394 Theurich, G., et al. (2016), The Earth System Prediction Suite: Toward a coordinated U.S.
1395 modeling capability, *Bull. Amer. Meteorol. Soc*., 97(7), 1229–1247, doi:10.1175/BAMS-D-14-
1396 00164.1.

1397 Thomas, E. G., J. B. H. Baker, J. M. Ruohoniemi, L. B. N. Clausen, A. J. Coster, J. C. Foster,
1398 and P. J. Erickson (2013), Direct observations of the role of convection electric field in the
1399 formation of a polar tongue of ionization from storm enhanced density, J. Geophys. Res. Space
1400 Phys., 118, 1180–1189; doi:10.1002/jgra.50116.

1401 Thomsen, M. F., J. E. Borovsky, D. J. McComas, R. C. Elphic, and S. Maurice (1998),
1402 Magnetospheric response to the CME passage of January 10 – 11, 1997, as seen at
1403 geosynchronous orbit, Geophys. Res. Lett., 25, 2545.

1404
1405 Thomsen, M. F., E. Noveroske, J. E. Borovsky, and D. J. McComas (1999), Calculation of the
1406 Moments From Measurements by the Los Alamos Magnetospheric Plasma Analyzer, LA-13566-
1407 MS, Los Alamos National Laboratory, Los Alamos, New Mexico.

1408
1409 Torr, M. R., D. G. Torr, P. G. Richards (1980a), The solar ultraviolet heating efficiency of the
1410 midlatitude thermosphere, J. Geophys. Res., https://doi.org/10.1029/GL007i005p00373.
1411
1412 Torr, M. R., P. G. Richards, D. G. Torr, (1980b), A new determination of the ultraviolet heating
1413 efficiency of the thermosphere, J. Geophys. Res., https://doi.org/10.1029/JA085iA12p06819.

1414

1415
1416 Torr, M. R., D. G. Torr, P. G. Richards, and S. P. Yung (1990), Mid- and low-latitude model of
1417 thermospheric emissions, 1, O+(2P) 7320 Å and N2(2P) 3371 Å, J. Geophys. Res., 95, 21,147–
1418 21,168.
1419
1420 Tsurutani, B. T., et al. (2004), Global dayside ionospheric uplift and enhancement associated
1421 with interplanetary electric fields, *J. Geophys. Res*., 109, A08302, doi:10.1029/2003JA010342

1422
1423 Vierinen, J., Coster, A. J., Rideout, W. C., Erickson, P. J., and Norberg, J. (2015). Statistical
1424 framework for estimating GNSS bias, Atmospheric Measurement Techniques
1425 Discussions,8(9),9373--9398, http://doi:10.5194/amt-9-1303-2016.

Walsh, B. M., D. G. Sibeck, Y. Nishimura, and V. Angelopoulos (2013), Statistical analysis of the plasmaspheric plume at the magnetopause, J. Geophys. Res. Space Physics, 118, 4844–4851, doi:10.1002/jgra.50458.

Walsh, B. M., J. C. Foster, P. J. Erickson, and D. G. Sibeck (2014), Simultaneous ground- and space-based observations of the plasmaspheric plume and reconnection, Science, 343(6175), 1122–1125; doi:10.1126/science.1247212.

Weimer, D. R. (1996). A flexible, IMF dependent model of high-latitude electric potentials having "space weather" applications. Geophysical Research Letters, 23(18), 2549–2552. https://doi.org/10.1029/96GL02255

Weiss, L. A., R. L. Lambour, R. C. Elphic, and M. F. Thomsen (1997), Study of plasmaspheric evolution using geosynchronous observations and global modeling, Geophys. Res. Lett., 24, 599.

Yizengaw, E., J. Dewar, J. MacNeil, M. B. Moldwin, D. Galvan, J. Sanny, D. Berube, and B. Sandel (2008), The occurrence of ionospheric signatures of plasmaspheric plumes over different longitudinal sectors, J. Geophys. Res., 113, A08318, doi:10.1029/2007JA012925.

Young. E. R., P. G. Richards, and D. G. Torr (1980a) A flux preservation method of coupling first and second order equations to simulate the flow of plasma between the protonosphere and ionosphere, J. Comput. Phys., 38, 141.

Young. E. R. D. G. Torr, P. G. Richards, and A. F. Nagy (1980b) A computer simulation of the midlatitude plasmasphere and ionosphere. Planet. Space Sci., 28, 881.

Yuan, Z., L. Zhao, Y. Xiong, X. Deng, and J. Wang (2011), Energetic particle precipitation and the influence on the sub-ionosphere in the SED plume during a super geomagnetic storm, *J. Geophys. Res*., 116, A09317, doi:10.1029/2011JA016821

Zou, S., A. J. Ridley, M. B. Moldwin, M. J. Nicolls, A. J. Coster, E. G. Thomas, and J. M. Ruohoniemi (2013), Multi-instrument observations of SED during 24–25 October 2011 storm: Implications for SED formation processes, *J. Geophys. Res.: Space Physics*, 118, 7798–7809, doi:10.1002/2013JA018860

Figure 1. (A) Solar wind velocity, (B) total interplanetary magnetic field (IMF), field $|B|$ measured by the Wind and ACE spacecraft (black curve), and IMF geocentric solar magnetospheric (GSM) components measured at L1 (~1.42×10^6 km from Earth, time-shifted to the sub-solar magnetopause location) IMF B_z component (red curve), and IMF B_y, component (green curve); (C) estimated polar cap potential drop (black curve); (D) SYM-H index, during 17 March 2013 (a) and 2015(b).

Figure 2a–**c**. THEMIS magnetopause crossings during which cold, dense plume plasma was observed near the dayside magnetopause for the three spacecraft: (a)ThA; (b)ThD; and (c)ThE. The panels from top to bottom present: (A) magnetic field vector components; (B) electron density from spacecraft potential; (C) dawn-to-dusk electric field; (D) ion energy flux; (E) electron energy flux for the 17 March 2015 storm. The vertical solid lines indicate the magnetopause crossing.

Figure 3a–**b**. The THEMIS spacecraft orbit at 1800 UT 17 Mar—2000UT 17 Mar 2015 in the X-Y plane (a) and the X-Z plane (b) in GSM coordinates. The orbit has its apogee in the dayside. The inbound and outbound are respectively in the nightside and the dayside.

Figure 4. Ionospheric plumes observed by GPS-TEC observations during the St. Patrick's Day storms on 17 Mar:(a) northern hemisphere at 1900UT in 2013; (b) same time as (a) but southern hemisphere;(c) northern hemisphere at 1930UT in 2015. The color scales show TEC units (TECU) where 1 TECU = 10^{16} electrons/m^2. The time integration of data was made for 15 minutes in order to gain more spatial coverage of the data points. The plots are oriented so that local noon is up for the northern hemisphere, while local midnight is up for the southern hemisphere. The three letters (A, D, and E) in Figure 4c show the magnetic footprints of the three THEMIS satellites as they crossed the reconnecting magnetopause, as shown in Figure 2a–c.

Figure 5. Ionospheric plumes in TEC reproduced by the IPE model simulations on 17 Mar, 2013 at the same time as the GPS-TEC observations in Figure 4:(a) northern hemisphere at 1900UT (b) same time as (a) but southern hemisphere; (c)northern hemisphere at 1930UT on 2015-03-17. The arrows on the IPE-TEC display the corresponding plasma flows from the IPE model simulations.

Figure 6. Plasmaspheric cold ion density [cm^{-3}] (a,c) and ion speed [m/s] (b,d) observed by the LANL MPA instruments at L=6.6, as functions of MLT and DOY counting from 11 March (a-b) in 2013; (c-d) in 2015.

Figure 7. Cold ion velocity vector plot from 17 Mar to 18 Mar in 2015. The color shows the corresponding cold ion density.

Figure 8. Plasmaspheric cold ion density [cm^{-3}] at L=6.6 calculated by the IPE model simulations as functions of MLT and DOY counting from 00UT of 17 March (a) 2013; (b) 2015.

Figure 9. Plasmaspheric electron density [cm^{-3}] at the magnetospheric equatorial plane calculated by the IPE model simulations on 17 March, at the same time of the TOI plumes in Figure 5: (a) 1900UT in 2013; (b) 1930UT in 2015.

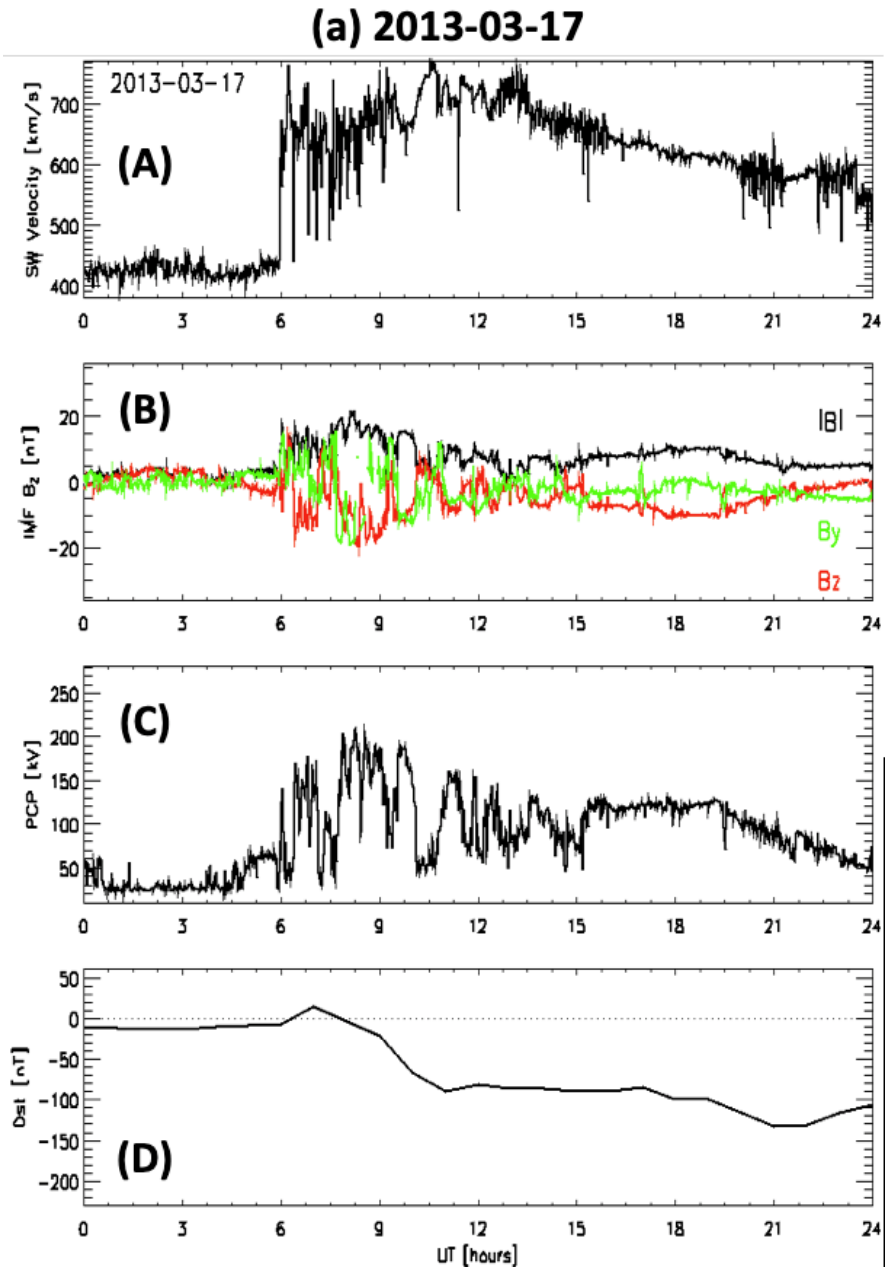

1497

1498 **Figure 1a**. (A) Solar wind velocity, (B) total interplanetary magnetic field (IMF), field $|B|$
1499 measured by the Wind and ACE spacecraft (black curve), and IMF geocentric solar
1500 magnetospheric (GSM) components measured at L1 (~1.42×10^6 km from Earth, time-shifted to
1501 the sub-solar magnetopause location) IMF B_z component (red curve), and IMF B_y component
1502 (green curve); (C) estimated polar cap potential drop (black curve); (D) SYM-H index, during 17
1503 March 2013 (a) and 2015(b).

1504

1505

1506

1507

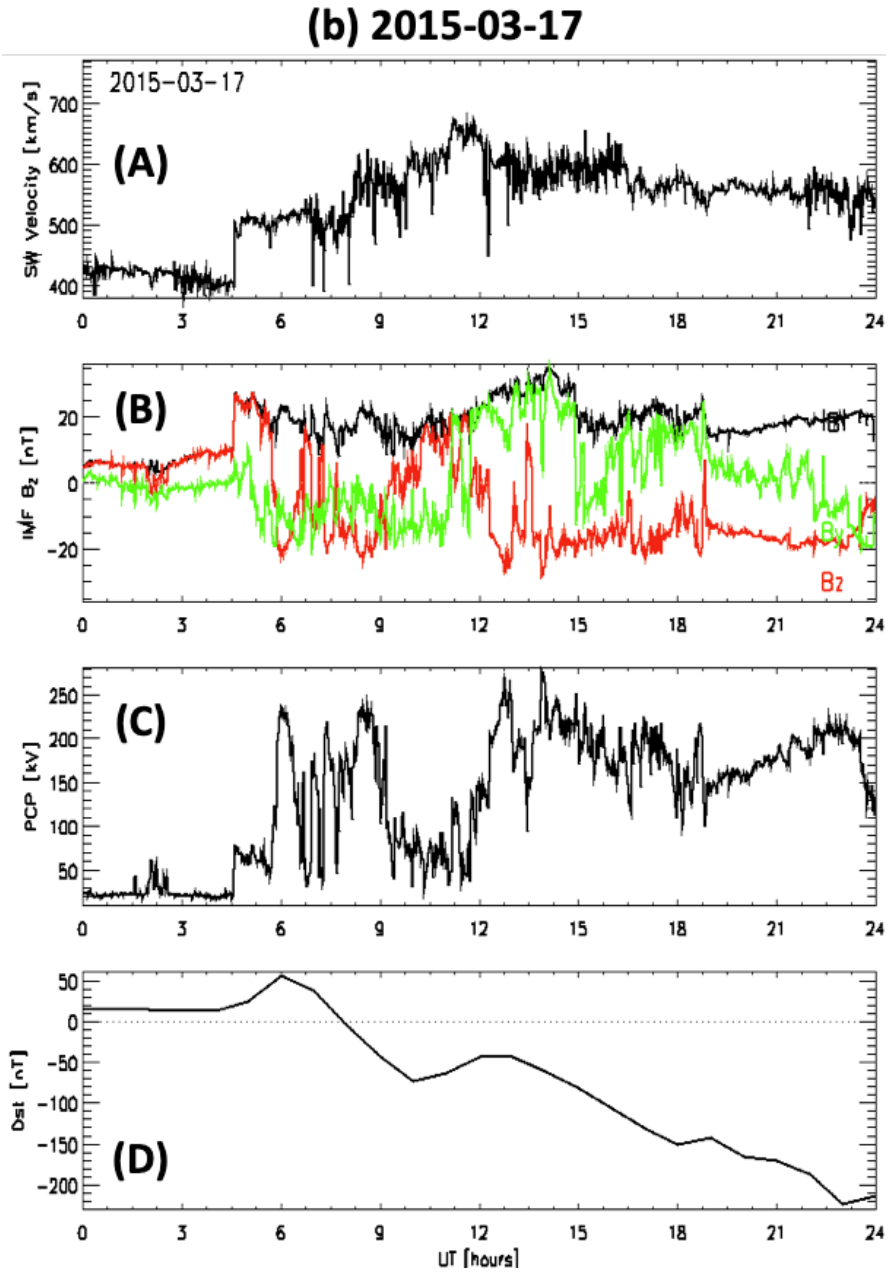

1508

1509 **Figure 1b**. (A) Solar wind velocity, (B) total interplanetary magnetic field (IMF), field $|B|$
1510 measured by the Wind and ACE spacecraft (black curve), and IMF geocentric solar
1511 magnetospheric (GSM) components measured at L1 (~1.42×10^6 km from Earth, time-shifted to
1512 the sub-solar magnetopause location) IMF B_z component (red curve), and IMF B_y, component
1513 (green curve); (C) estimated polar cap potential drop (black curve); (D) SYM-H index, during 17
1514 March 2013 (a) and 2015(b).
1515

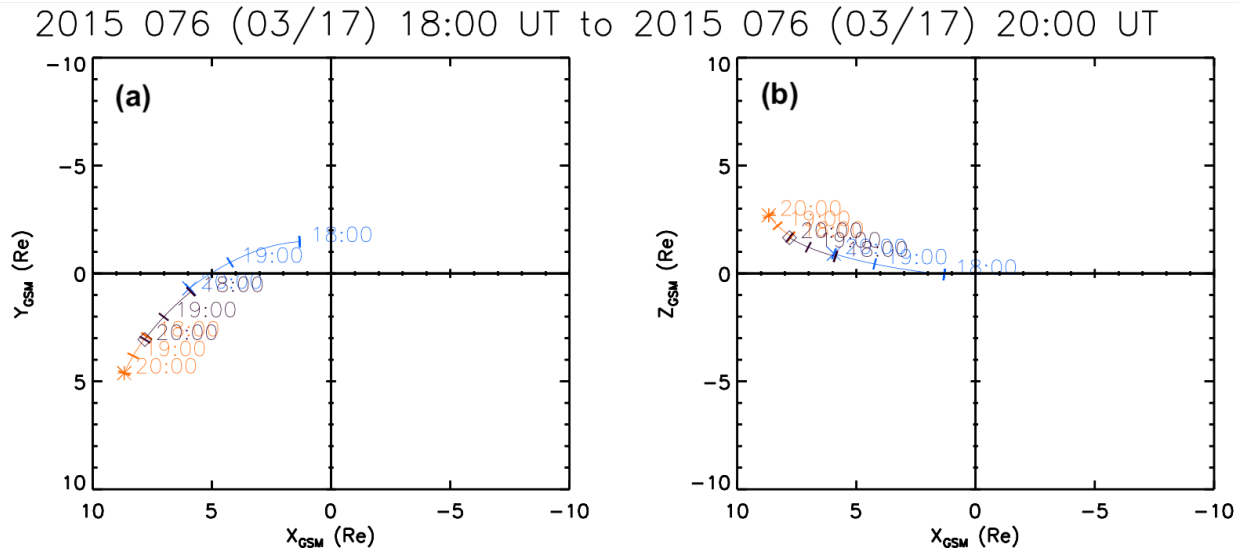

Figure 2a–**b**. The THEMIS spacecraft orbit at 1800 UT 17 Mar—2000 UT 17 Mar 2015 in the X-Y plane (a) and the X-Z plane (b) in the GSM coordinates. The orbit has its apogee in the dayside. The inbound and outbound are respectively in the nightside and the dayside.

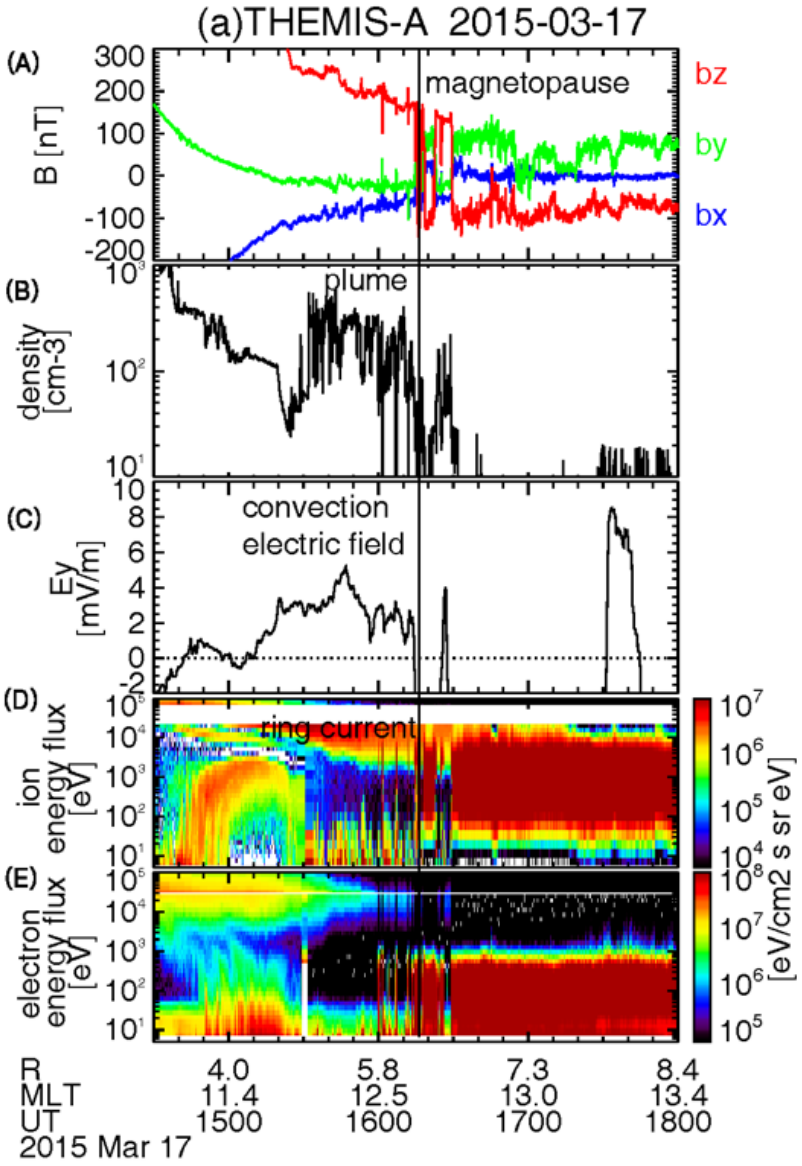

Figure 3a. THEMIS magnetopause crossings during which cold, dense plume plasma was observed near the dayside magnetopause for the three spacecraft: (a)ThA; (b)ThD; and (c)ThE. The panels from top to bottom present: (A) magnetic field vector components; (B) electron density from spacecraft potential; (C) dawn-to-dusk electric field; (D) ion energy flux; (E) electron energy flux for the 17 March 2015 storm. The vertical solid lines indicate the magnetopause crossing.

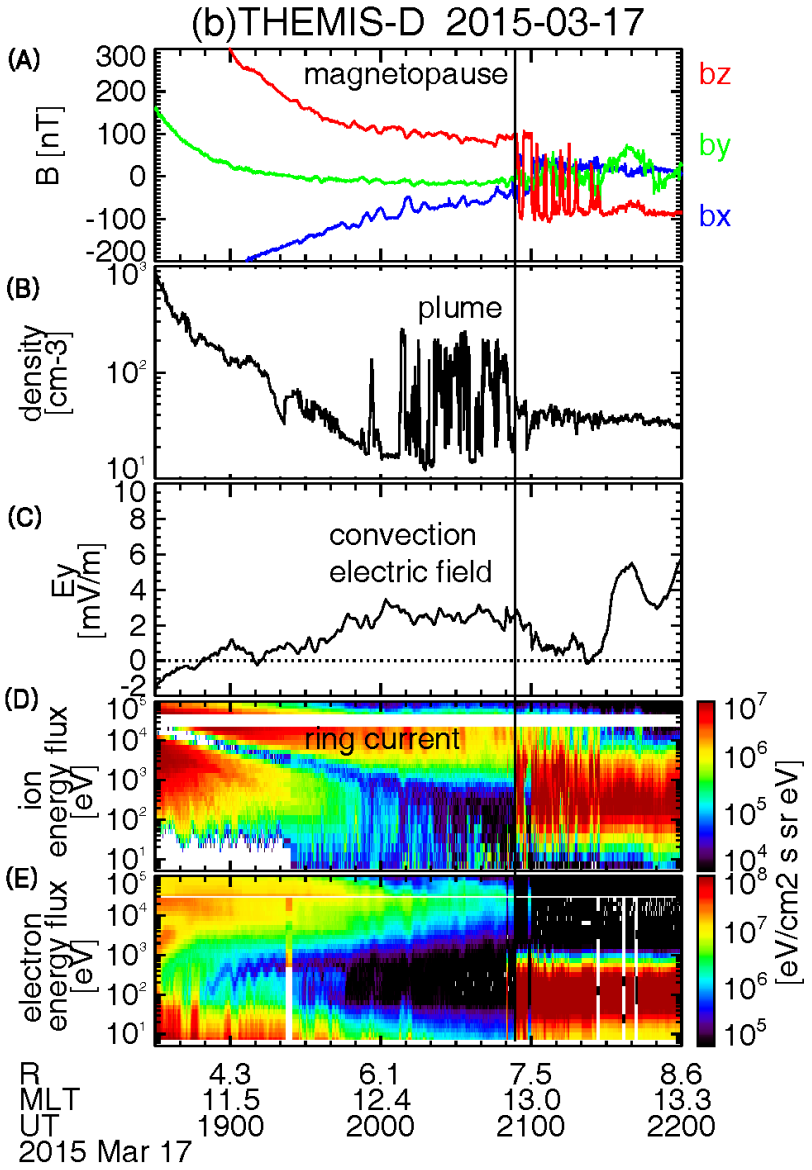

1529

1530 **Figure 3b**. THEMIS magnetopause crossings during which cold, dense plume plasma was observed near
1531 the dayside magnetopause for the three spacecraft: (a)ThA; (b)ThD; and (c)ThE. The panels from top to
1532 bottom present: (A) magnetic field vector components; (B) electron density from spacecraft potential; (C)
1533 dawn-to-dusk electric field; (D) ion energy flux; (E) electron energy flux for the 17 March 2015 storm.
1534 The vertical solid lines indicate the magnetopause crossing.
1535

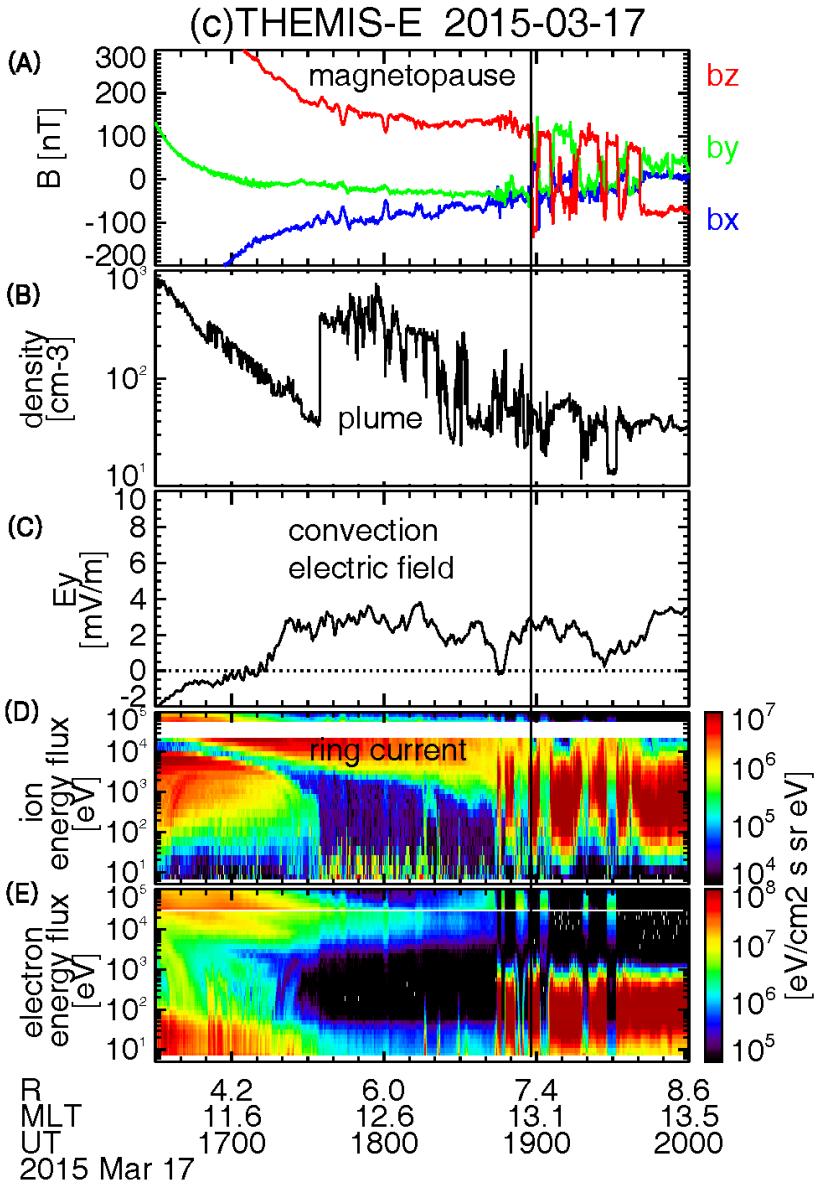

Figure 3c. THEMIS magnetopause crossings during which cold, dense plume plasma was observed near the dayside magnetopause for the three spacecraft: (a)ThA; (b)ThD; and (c)ThE. The panels from top to bottom present: (A) magnetic field vector components; (B) electron density from spacecraft potential; (C) dawn-to-dusk electric field; (D) ion energy flux; (E) electron energy flux for the 17 March 2015 storm. The vertical solid lines indicate the magnetopause crossing.

1543 Figure 4a–b

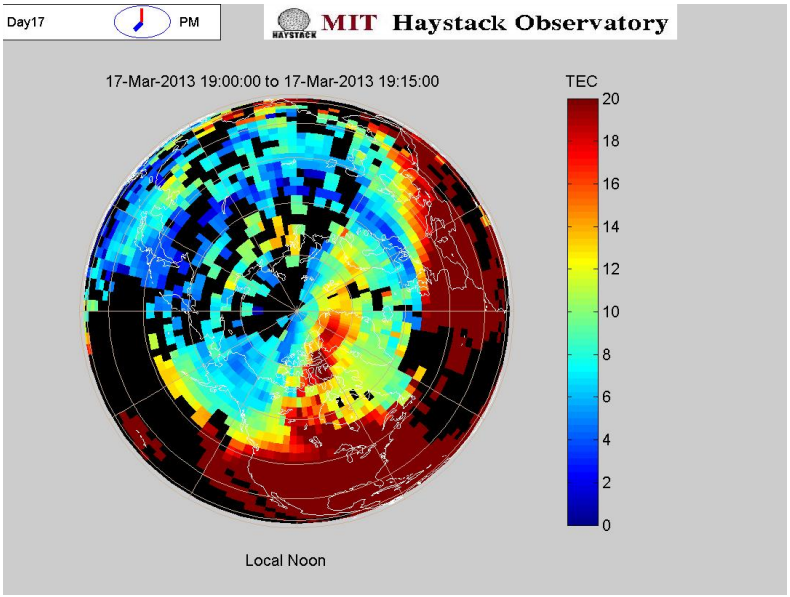

1544

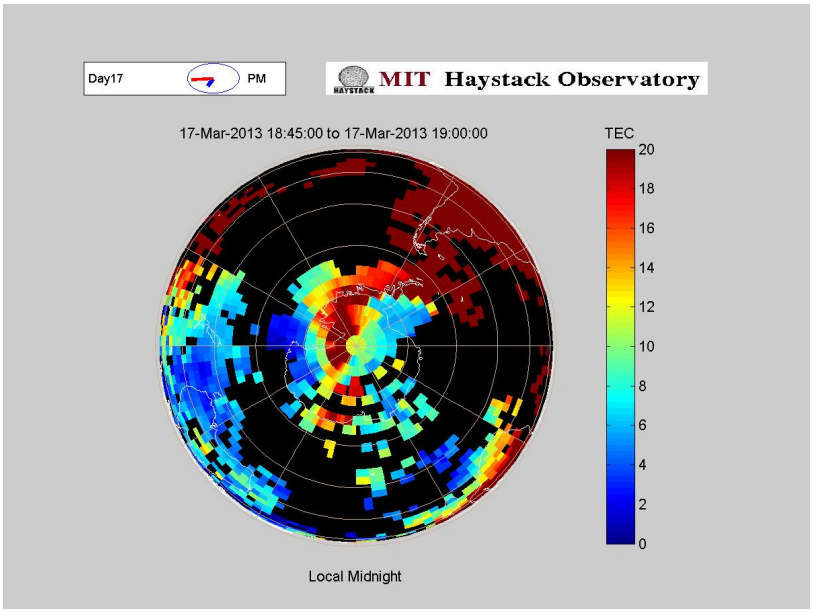

1545

1546 **Figure 4a–b**. Ionospheric plumes observed by GPS-TEC observations during the St. Patrick's Day
1547 storms on 17 Mar:(a) northern hemisphere at 1900UT in 2013; (b) same time as (a) but southern
1548 hemisphere. The color scales show TEC units (TECU) where 1 TECU = 10^{16} electrons/m^2. The data was
1549 integrated over 15 minutes in order to gain more spatial coverage of the TOI/SED features. The plots are
1550 oriented so that local noon is up for the northern hemisphere, while local midnight is up for the southern
1551 hemisphere.
1552

Figure 4c

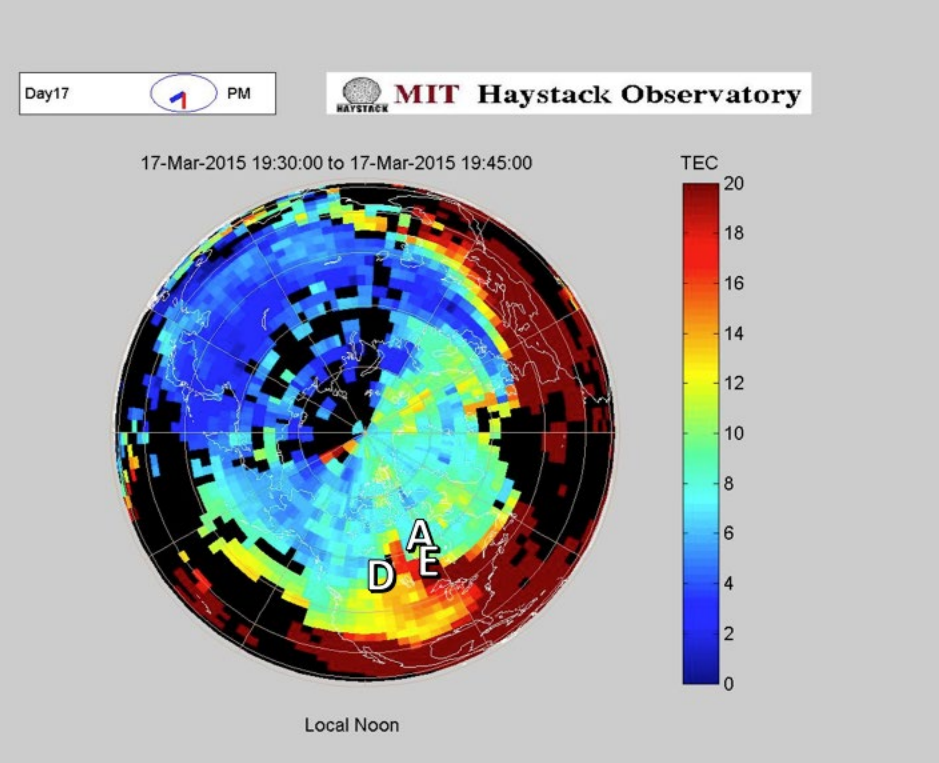

Figure 4c. Ionospheric plumes observed by GPS-TEC observations during the St. Patrick's Day storms on 17 Mar:(c) northern hemisphere at 1930UT in 2015. The color scales show TEC units (TECU) where 1 TECU = 10^{16} electrons/m^2. The data was integrated over 15 minutes in order to gain more spatial coverage of the TOI/SED features. The plots are oriented so that local noon is up for the northern hemisphere, while local midnight is up for the southern hemisphere. The three letters (A, D, and E) in Figure 4c show the magnetic footprints of the three THEMIS satellites as they crossed the reconnecting magnetopause, as shown in Figure 2a–c.

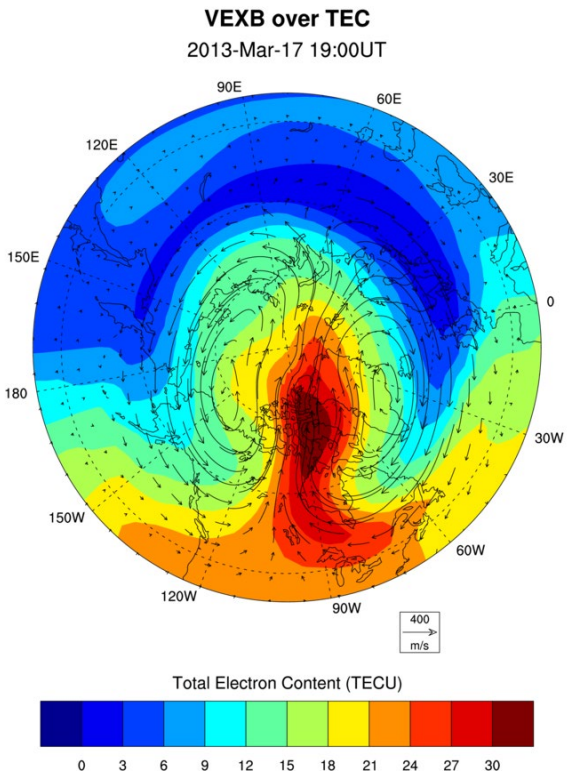

Figure 5. Ionospheric plumes in TEC reproduced by the IPE model simulations on 17 Mar, 2013 at the same time as the GPS-TEC observations in Figure 4:(a) northern hemisphere at 1900UT (b) same time as (a) but southern hemisphere; (c) northern hemisphere at 1930UT on 2015-03-17. The arrows on the IPE-TEC display the corresponding plasma flows from the IPE model simulations.

1572 Figure 5b–c

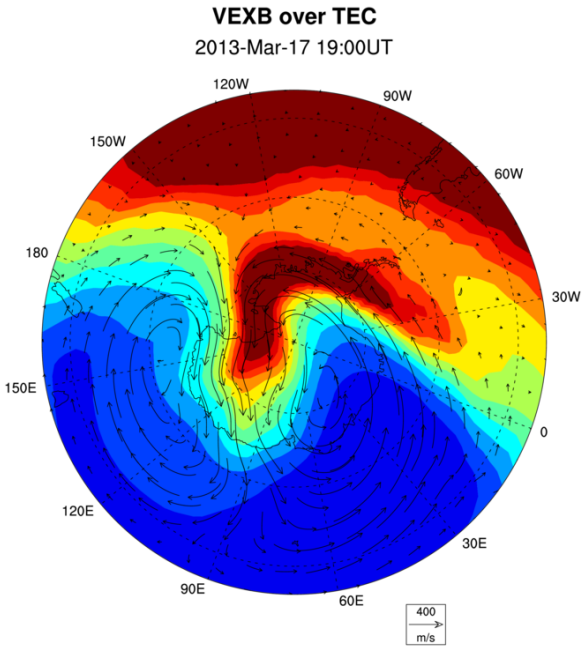

1573

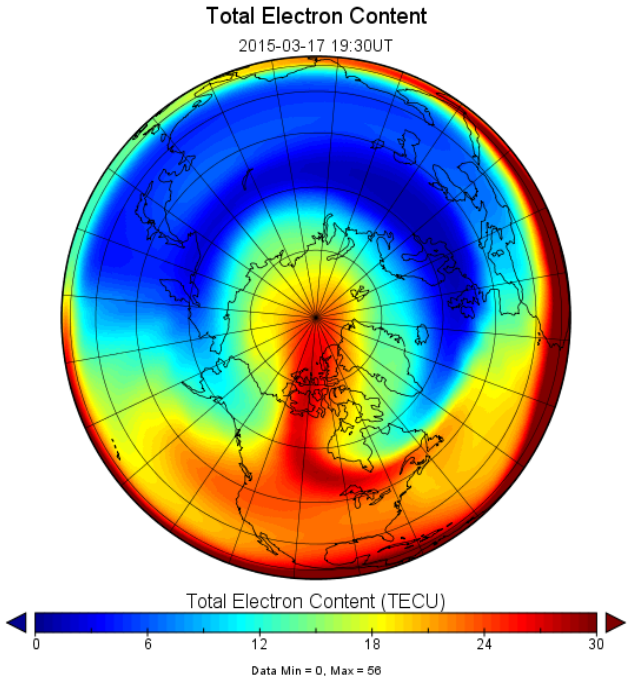

1574

1575 **Figure 5**. Ionospheric plumes in TEC reproduced by the IPE model simulations on 17 Mar, 2013 at the
1576 same time as the GPS-TEC observations in Figure 4:(a) northern hemisphere at 1900UT (b)same time as

(a) but southern hemisphere; (c) northern hemisphere at 1930UT on 2015-03-17. The arrows on the IPE-TEC display the corresponding plasma flows from the IPE model simulations.

1580 Figure 6a–d

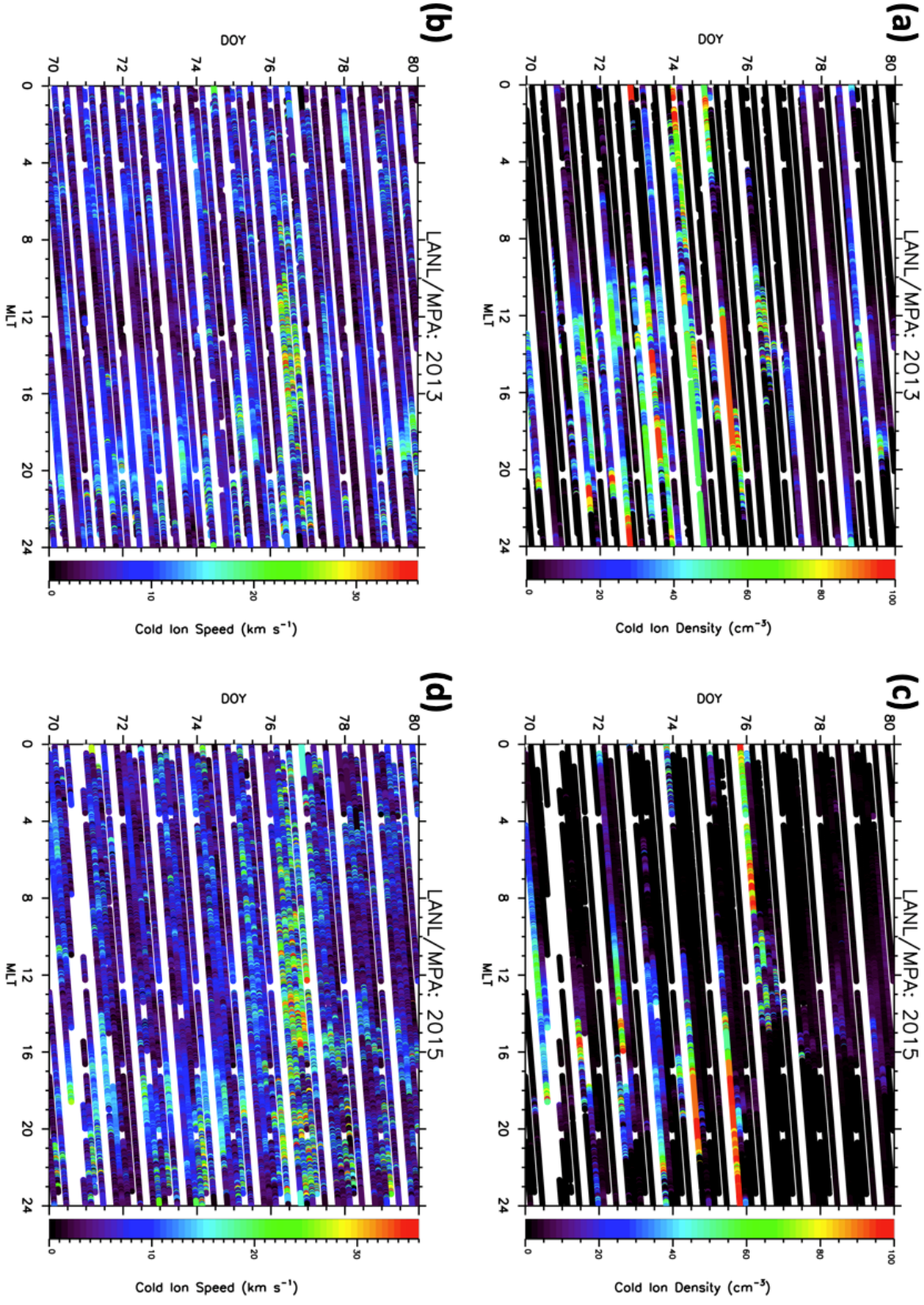

1581

1582 **Figure 6**. Plasmaspheric cold ion density [cm^{-3}] (a,c) and ion speed [m/s] (b,d) observed by the LANL
1583 MPA instruments at L=6.6, as functions of MLT and DOY counting from 11 March (a-b) in 2013; (c-d)
1584 in 2015.
1585

1586 Figure 7

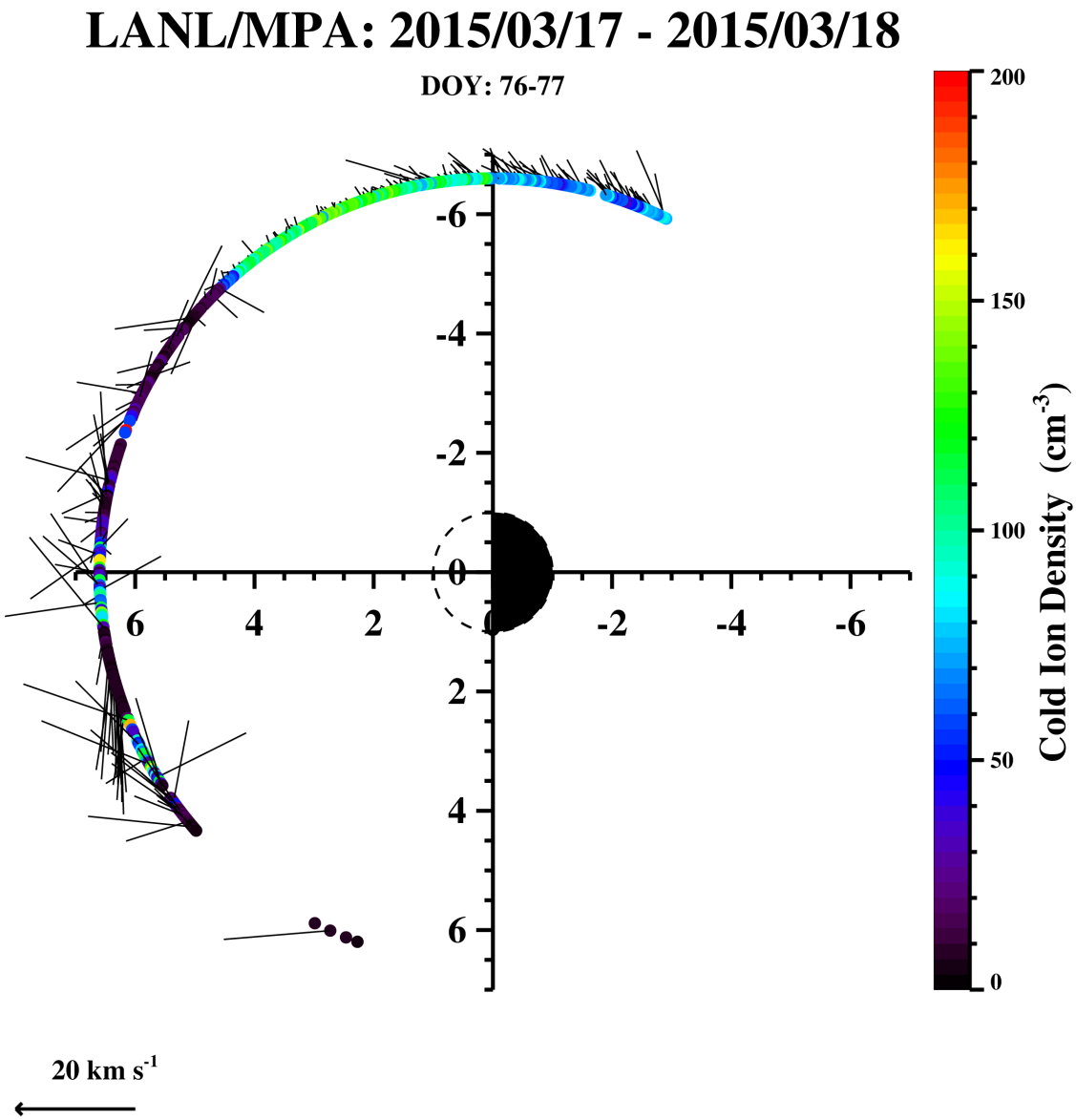

1587

1588 **Figure 7**. Cold ion velocity vector plot from 17 Mar to 18 Mar in 2015. The color shows the
1589 corresponding cold ion density.
1590

1591 Figure 8a–b

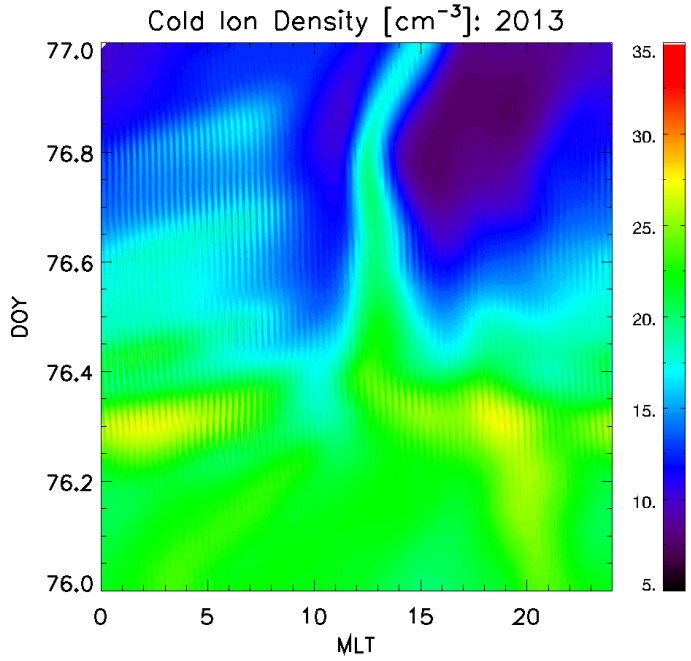

1592

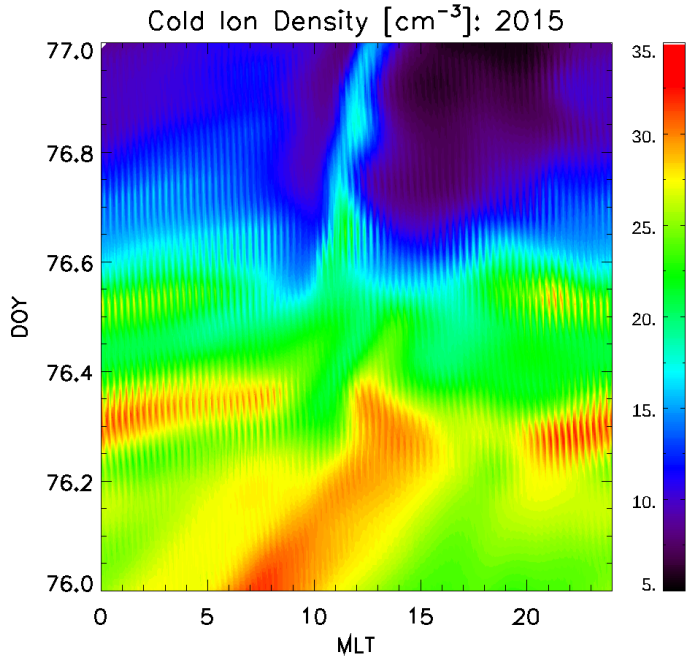

1593

1594 **Figure 8**. Plasmaspheric cold ion density [cm^{-3}] at L=6.6 calculated by the IPE model simulations as
1595 functions of MLT and DOY counting from 00UT of 17 March (a) 2013; (b) 2015.
1596

1597 Figure 9a–b

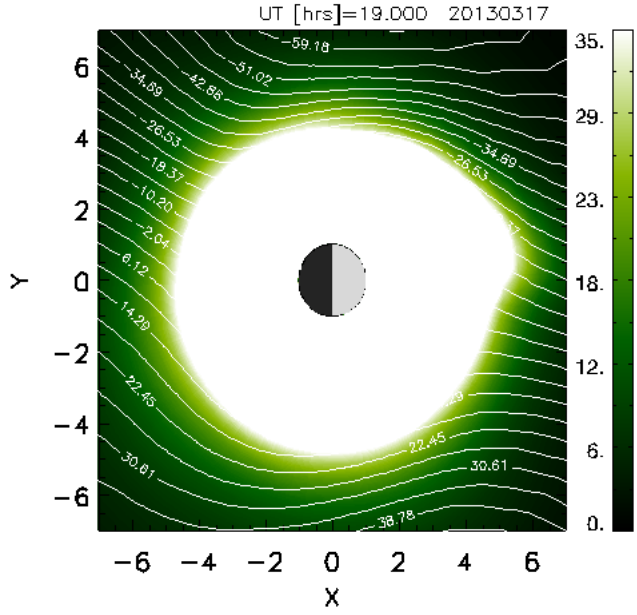

1598

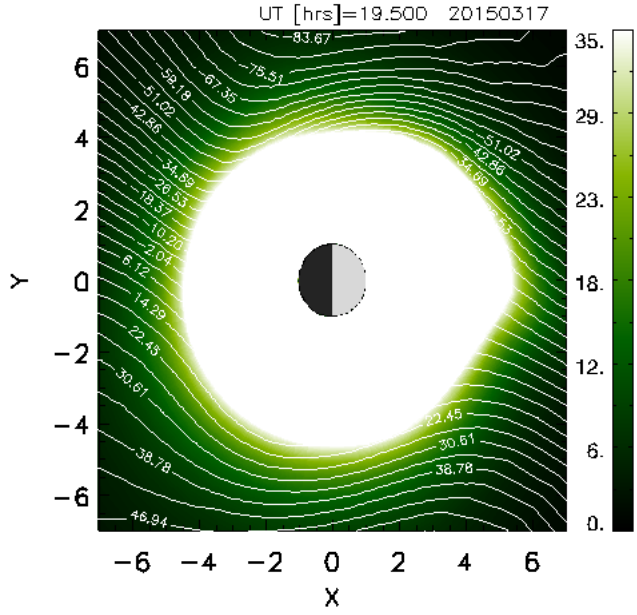

1599

1600 **Figure 9**. Plasmaspheric electron density [cm^{-3}] at the magnetospheric equatorial plane calculated by the
1601 IPE model simulations on 17 March, at the same time of the ionospheric plumes in Figure 5: (a) 1900UT
1602 in 2013; (b) 1930UT in 2015